# On the Changes in Convection-Allowing WRF Forecasts of MCS Evolution due to Decreases in Model Horizontal and Vertical Grid Spacing. Part I: Changes in Cold Pool Evolution

BRIAN J. SQUITIERI[a] AND WILLIAM A. GALLUS JR.[a]

[a] *Department of Geological and Atmospheric Sciences, Iowa State University, Ames, Iowa*

ABSTRACT: The degree of improvement in convective representation in NWP with horizontal grid spacings finer than 3 km remains debatable. While some research suggests subkilometer horizontal grid spacing is needed to resolve details of convective structures, other studies have shown that decreasing grid spacing from 3–4 to 1–2 km offers little additional value for forecasts of deep convection. In addition, few studies exist to show how changes in vertical grid spacing impact thunderstorm forecasts, especially when horizontal grid spacing is simultaneously decreased. The present research investigates how warm-season central U.S. simulated MCS cold pools for 11 observed cases are impacted by decreasing horizontal grid spacing from 3 to 1 km, while increasing the vertical levels from 50 to 100 in WRF runs. The 3-km runs with 100 levels produced the deepest and most negatively buoyant cold pools compared to all other grid spacings since updrafts were more poorly resolved, resulting in a higher flux of rearward-advected frozen hydrometeors, whose melting processes were augmented by the finer vertical grid spacing, which better resolved the melting layer. However, the more predominant signal among all 11 cases was for more expansive cold pools in 1-km runs, where the stronger and more abundant updrafts focused along the MCS leading line supported a larger volume of concentrated rearward hydrometeor advection and resultant latent cooling at lower levels.

KEYWORDS: Cold pools; Convective storms/systems; Mesoscale systems; Mesoscale forecasting; Numerical weather prediction/forecasting; Cloud resolving models

## 1. Introduction

At present, atmospheric scientists continue to question how fine model grid spacing needs to be to sufficiently resolve deep moist convection for forecasting purposes at a reasonable computational cost. Decreasing horizontal grid spacing ($\Delta x$) down to 3–4 km in NWP can explicitly resolve MCS structures (Done et al. 2004; Weisman et al. 2008), hence such grid spacings are currently employed in most convection allowing models (CAMs). However, it is unclear if $\Delta x$ should be decreased to less than 3–4 km to optimally resolve MCS structures in numerical forecasts, especially when considering the greatly increased computational expenses. Idealized squall-line studies have shown that subkilometer $\Delta x$ simulations best represent observations (Bryan and Morrison 2012), while aggregate studies of multiple real-cases of deep moist convection have shown that decreasing $\Delta x$ past 3 km adds little qualitative value to forecasts (Kain et al. 2008; Clark et al. 2012) or contributes statistically insignificant improvement to MCS structural representation or forecast skill (Thielen and Gallus 2019; Squitieri and Gallus 2020). Few studies, however, have explored the consequences of decreasing vertical grid spacing ($\Delta z$) in CAMs in deep-moist convective simulations. Lebo and Morrison (2015) noted that for both the convection-allowing and large-eddy simulation $\Delta x$ regimes of a simulated idealized squall line, changes in $\Delta z$ had little impact on squall-line structure compared to what happened with $\Delta x$ changes, though it was believed that

surface fluxes in real-case runs may introduce more sensitivity in deep convective structural representation with $\Delta z$ changes.

MCSs are known often to be self-organizing phenomena (Parker 2021), where morphology and longevity are highly dependent on internal storm-scale circulations (Newton 1950; Zipser 1982; Parker and Johnson 2000) and the development of a convectively generated cold pool (Marsham et al. 2011; Miller et al. 2020; Parker et al. 2020; Parker 2021). MCS forward propagation is often driven by the cold pool (Coniglio et al. 2006; Parker 2008; Billings and Parker 2012), contributing directly to MCS speed (Charba 1974; Newton and Fankhauser 1975; Betts 1976; Miller and Betts 1977), direction (Corfidi et al. 1996; Corfidi 2003; Tuttle and Carbone 2004), intensity (Mallinson and Lasher-Trapp 2019; Borque et al. 2020), and longevity (Wilhelmson and Chen 1982; Rotunno et al. 1988), so resolving cold pool structures with adequate $\Delta x$ and $\Delta z$ is vital to accurately simulate MCSs. Microphysics (MP) have been found to play an equally important role in MCS cold pool evolution relative to other model parameterizations and configurations (Li et al. 2009a,b; Van Weverberg et al. 2012; Adams-Selin et al. 2013a,b; Fan et al. 2017; Bao et al. 2019; Mallinson and Lasher-Trapp 2019). Melting frozen hydrometeors and evaporating liquid species in the MCS trailing precipitation region contribute greatly to MCS and cold pool evolution (Leary and Houze 1979; Rutledge and Houze 1987; Caniaux et al. 1994; Braun and Houze 1995; Gallus and Johnson 1995a,b). As such, it may be hypothesized that under constant fall speeds, hydrometeor phase change and latent heat release magnitudes in finer $\Delta z$ runs may increase compared to coarser $\Delta z$ runs as both liquid and ice species would be falling across more model vertical levels,

*Corresponding author*: Brian Squitieri, brianjs@iastate.edu

better resolving phase changes, particularly in or near the melting layer.

Previous studies have found that smaller but more intense updrafts in greater numbers comprised better-resolved squall line structure in finer $\Delta x$ runs (Bryan et al. 2003; Bryan and Morrison 2012; Lebo and Morrison 2015; Verrelle et al. 2015), which was the inference made by Squitieri and Gallus (2020) as to why finer $\Delta x$ cold pools were overall more intense and expansive. The present study expands on Squitieri and Gallus (2020) by refining $\Delta x$ and $\Delta z$ to see if larger numbers of stronger updrafts, generated by finer grid spacings, contribute to more expansive cold pools through greater rearward hydrometeor advection into the downdraft region, supporting more microphysical cooling. It was hypothesized that a greater updraft number and intensity generates larger areas of ice and liquid hydrometeor production in finer $\Delta x$ runs, which in turn supports greater coverage of microphysical cooling, resulting in a more expansive cold pool with greater leading-line ascent, recently inferred in a convective cold pool study by Hirt et al. (2020). Another goal was to see if cold pools became deeper and stronger by the better resolution of melting layer microphysical processes, where stronger latent cooling via greater frozen hydrometeor melting and liquid hydrometeor evaporation would occur with finer $\Delta z$. Since real cases are simulated in a heterogeneous environment with surface fluxes taken into account, it is believed that $\Delta z$ sensitivities would be more prevalent in MCS structural representation than in Lebo and Morrison (2015).

Section 2 of this manuscript reviews the model configurations, cold pool calculations, statistical methods and experimental setup used to derive results. Section 3 discusses results, with the summary and discussion section comprising section 4.

## 2. Methodology

### a. Case selection

In total, 11 observed MCSs were selected for the present work, which were warm-season events (as in Coniglio et al. 2010) that occurred in the central United States (Table 1). Like Squitieri and Gallus (2020), the cases chosen were primarily nocturnal in nature, and eight of the cases chosen were not featured in Squitieri and Gallus (2020). Mainly newer nocturnal, central U.S. cases were selected so results from a limited sample size could be corroborated with Squitieri and Gallus (2020) mostly independent of the influence from the few older cases. The MCSs were required to be leading line/trailing stratiform MCSs (as in Parker and Johnson 2000), with pristine ambient environments preceding the MCS. The goal for selecting pristine MCS environments was to simplify analyses by avoiding impacts from other storms (i.e., deep convection contaminating the warm sector). Observed mosaic 1 km above ground level (AGL) radar reflectivity, available hourly, was used to select the 11 cases and was subjectively compared to model simulated reflectivity. Observed radar data were derived from the Multi-Radar Multi-Sensor (MRMS) system (Smith et al. 2016) and were retrieved from the Iowa

TABLE 1. A list of the 11 observed cases studied, featuring case number, date, observed MCS initiation time, and states primarily impacted. Cases highlighted with a "*" were also studied in Squitieri and Gallus (2020).

| Case No. | Date | Initiation time (UTC) | States impacted |
|---|---|---|---|
| 1 | 1 Jun 2018 | 2300 | NE, IA, KS, MO |
| 2 | 3 Jun 2015* | 0100 | NE, SD, IA |
| 3 | 9 Jun 2018 | 0100 | NE, SD |
| 4 | 16 Jun 2019 | 0100 | OK, TX |
| 5 | 28 Jun 2020 | 0200 | KS, NE, IA, MO |
| 6 | 5 Jul 2016 (north)* | 2200 | MN, IA, WI, IL |
| 7 | 6 Jul 2016 (south) | 0400 | KS |
| 8 | 7 Jul 2016* | 0000 | NE, SD, MN, IA, KS |
| 9 | 9 Jul 2020 | 0200 | NE, KS |
| 10 | 30 Jul 2018 | 0400 | KS, OK |
| 11 | 12 Aug 2019 | 0100 | NE, KS, IA |

Environment Mesonet data archives (Iowa Environmental Mesonet 2020).

Simulated MCS initiation times (t0) were subjectively defined at the hour when a 75–100-km-long coherent leading line of 50+ dB$Z$ and region of lighter trailing reflectivity was first observed (as in Parker and Johnson 2000; Gallus et al. 2008; Squitieri and Gallus 2020). Only the simulated MCSs with varying grid spacings are compared with each other in Part I of this research, with comparisons to observations made in Squitieri and Gallus (2022, hereafter Part II). Because hour of MCS initiation rarely differed among different grid-spacing configurations, t0 was treated as being the same for all grid spacings for a given MP scheme.

### b. Model setup and output

The WRF-ARW Model setup (Table 2) was like Squitieri and Gallus (2020), but with a few key differences. First, the 3-km parent domain was 2250 × 2250 km², and with no 0.333-km nest included, but with the same sized (1000 × 1000 km²) 1-km one-way nested domain (Fig. 1). This was necessary to reduce computational costs associated with simulating MCSs with 50 and 100 levels on the CISL-Cheyenne supercomputing system (CISL 2020). WRF-ARW version 4.2 (Skamarock et al. 2019a) was selected for this experiment in place of version 3.8 (Skamarock et al. 2008), since modifications were made to the Thompson MP scheme based on observations from Field et al. (2019) in version 4.2 to better calibrate the intercept parameter and associated graupel mixing ratio relationship (Werner and UCAR 2020).

The WRF-ARW employs a stretched vertical grid with terrain-following eta coordinates that are nonlinearly spaced through the troposphere (Skamarock et al. 2019a). All runs in this experiment incorporate roughly $\Delta z \approx 100$–150 m in the lowest 1500 m (Fig. 2). The 50 default vertical levels above the boundary layer generally correspond to $\Delta z \approx 400$–550 m. For increasing vertical levels in this study, it was most feasible to double the eta vertical coordinates to 100 vertical levels, which translates to $\Delta z \approx 200$–250 m at altitudes above 1 km AGL. Since $\Delta z$ was already relatively fine in the PBL, no

TABLE 2. Model configurations used for WRF-ARW v4.2 simulations.

| WRF-ARW 4.2 | Configuration | Reference |
|---|---|---|
| Initial conditions | NAM-218 (12-km grid) | NOAA/NCDC (2015) |
| Initialization time | 1200 UTC | — |
| End time | 1200 UTC | — |
| Total time | 24 h | — |
| Temporal output | Hourly | — |
| Time step (3-km domain—$dt$) | 6 s | — |
| Model top | 50 hPa | — |
| Horizontal grid spacing ($\Delta x$) | 3 km, 1 km | — |
| No. of vertical levels | 50, 100 | — |
| Microphysics schemes | Thompson, WSM6 | Thompson et al. (2008); Hong and Lim (2006) |
| PBL scheme | MYJ | Janjić (1994) |
| Land surface | Noah-LSM | Chen and Dudhia (2001) |
| Shortwave radiation | Dudhia | Dudhia (1989) |
| Longwave radiation | RRTM | Mlawer et al. (1997) |

changes were made in this layer. Refining $\Delta z$ to roughly 200 m, even with $\Delta x = 3$ km, roughly matches the feasible $\Delta x/\Delta z$ ratio introduced by Skamarock et al. (2019b). Furthermore, refining $\Delta z$ above 1 km AGL satisfies the objective of better resolving the melting layer and associated microphysical processes internal to MCSs. In the present work, the four model grid spacings are known henceforth as 3 km–50 lev, 3 km–100 lev, 1 km–50 lev, and 1 km–100 lev.

Since MP scheme choices can heavily influence convective representation in CAM guidance (Adams-Selin et al. 2013a,b),

all WRF grid spacings were run with a part double-moment (Thompson) and single-moment (WSM6) MP scheme to assess how differences in representing graupel-based processes impact MCS and cold pool evolution with changing grid spacing. Microphysical tendencies that were identified in previous studies to highly influence MCS cold pool evolution were output as WRF variables with the intent to explain commonalities or differences in MCS cold pool representation with changing $\Delta x$ and $\Delta z$. The microphysical tendencies chosen to be evaluated were production of water vapor by rainfall evaporation, production of rainwater by melting graupel, and production of rainwater by melting snow. Since microphysical tendencies can vary considerably over any given time step, the tendencies were accumulated in hourly bins in the WRF MP drivers before being output. Upward and downward fluxes of hydrometeors were calculated to gauge if grid spacing changes influenced the distribution of liquid and ice species and
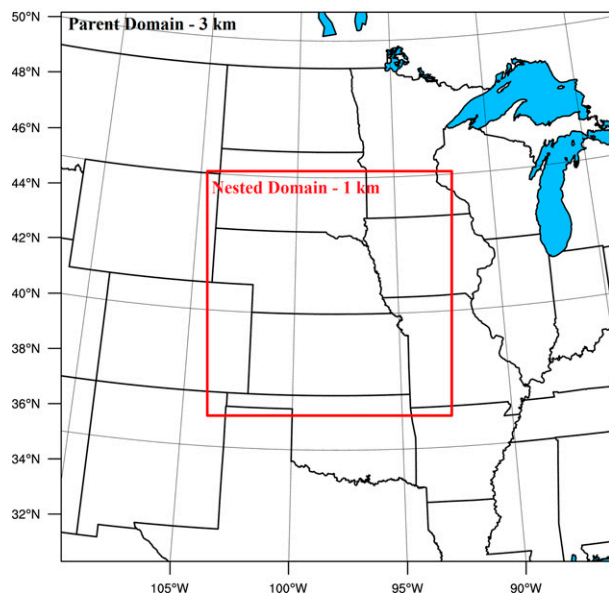


FIG. 1. Example of the WRF-ARW domain configuration for the 9 Jul 2020 case. The parent 3-km domain comprises an area of 2250 km × 2250 km, with the inner one-way nested 1-km domain covering 1000 km × 1000 km. While the center latitude and longitude placement for the domains varies per case and depends on the location of the observed MCS, the sizes and spatial arrangements of the 3- and 1-km domains are the exact same for all cases.
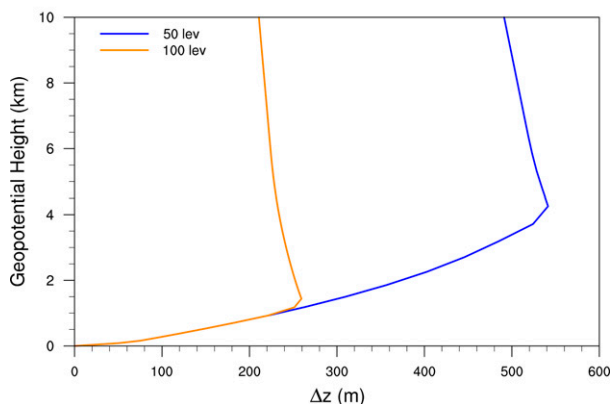


FIG. 2. A line graph depicting the vertical grid spacing ($\Delta z$; m) between WRF eta vertical levels, delineated by corresponding domain-averaged geopotential heights for runs employing 50 vertical levels (blue line) and 100 vertical levels (orange line). Geopotential heights were only plotted up to 10 km to adequately show how $\Delta z$ in runs employing 50 and 100 vertical levels varies with height and does not extend to the model top.
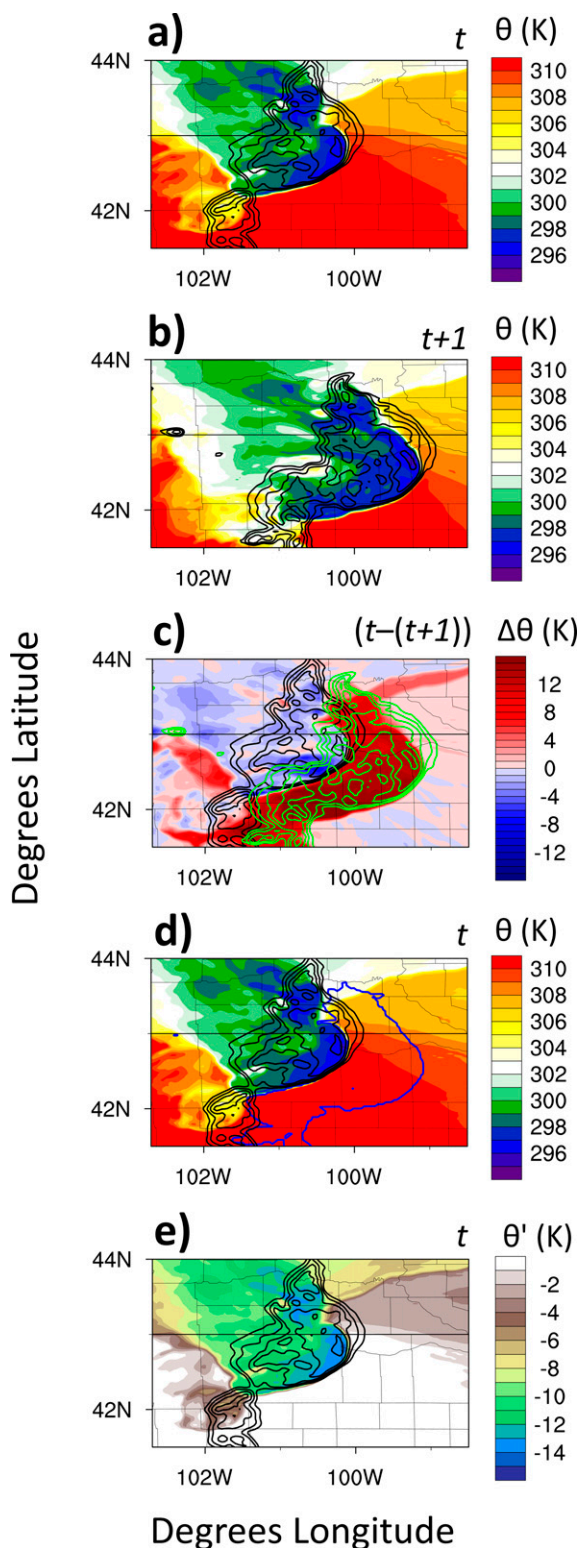
associated phase-change tendencies and in turn, impacted MCS cold pool evolution. Hydrometeor mixing ratios (kg kg$^{-1}$ or "unitless") were multiplied with the dry-air density (kg m$^{-3}$) to convert to a density, which was then multiplied with the vertical velocity field ($w$ in m s$^{-1}$) to produce upward and downward flux fields (units of $10^{-3}$ kg m$^{-2}$ s$^{-1}$) associated with the MCS updrafts and downdrafts. No positive or negative $w$ thresholds were applied since the hydrometeor (precipitation) flux fields are inherently related only to convection (i.e., the MCS).

### c. Cold pool calculations

As in many previous studies (e.g., Rotunno et al. 1988; Weisman 1992; Coniglio and Stensrud 2001; James et al. 2005; Bryan and Rotunno 2008; and Peters and Hohenegger 2017), the cold pool was evaluated by the integration of the convectively generated negative buoyancy acceleration, the cold pool parameter (m s$^{-1}$), calculated as

$$C^2 = 2\int_0^H (-B)\, dz, \tag{1}$$

where, like Squitieri and Gallus (2020), negative buoyancy ($-B$; m s$^{-2}$) was defined as

$$B \equiv g\left[\frac{\theta'}{\overline{\theta}} + 0.61(q_v - \overline{q}_v) - q_c - q_r\right], \tag{2}$$

where $H$ (m AGL) in (1) is the height where $B = 0$ m s$^{-2}$ or the height of the freezing level, whichever comes first. The variables $\overline{\theta}$ (K) and $\overline{q}_v$ (kg kg$^{-1}$) define the average potential temperature and water vapor mixing ratio, respectively, of the ambient pre-convective environment ahead of the MCS, determined in the following manner: For each time, at each vertical level on the native grid, the difference in potential temperature ($\Delta\theta$) at a given time $t$ (Fig. 3a) and $t + 1$ (Fig. 3b) was calculated at the 75th percentile to delineate the immediate ambient environment an MCS cold pool will move into (Fig. 3c). The ambient $\overline{\theta}$ and $\overline{q}_v$ were calculated by averaging the grid points comprising the 75th percentile $\Delta\theta$ area, and where composite reflectivity values exceeded 35 dB$Z$, ensuring that the strong temperature change was induced only by convective cold pools (Figs. 3c,d). The term $\theta'$ (K) is the negative perturbation potential temperature, calculated by subtracting $\overline{\theta}$ from the model potential temperature (K) field (Fig. 3e). In (2), $g$ is gravity (m s$^{-2}$), with $q_v$, $q_c$, and $q_r$ (kg kg$^{-1}$) being total water vapor, cloud water, and rainwater mixing

---

depicted by the surface potential temperature field (K, shaded), overlaid with the top 25% positive surface $\Delta\theta$ values between 2300 and 0000 UTC for grid points where the $t + 1$ composite reflectivity fields exceed 35 dB$Z$ (contoured in blue, which is averaged to a single value, $\overline{\theta}$). (e) Surface perturbation potential temperature (K; shaded), calculated by subtracting $\overline{\theta}$ from $\theta$. All plots are overlaid with composite reflectivity at time $t$ (black contours 35–65 dB$Z$, at intervals of 5), with (c) overlaid with contours of composite reflectivity at $t + 1$ (green contours 35–65 dB$Z$, at intervals of 5).

FIG. 3. Simulated surface cold pool associated with the 7 Jul 2016 MCS event employing 1 km–100 lev grid spacing. The cold pool at time (a) $t$ (2300 UTC) and (b) $t + 1$ (0000 UTC) is depicted by the potential temperature $\theta$ (K; shaded). (c) Surface $\Delta\theta$ fields $[t - (t + 1)]$ are shaded (K). (d) The cold pool at time $t$ is
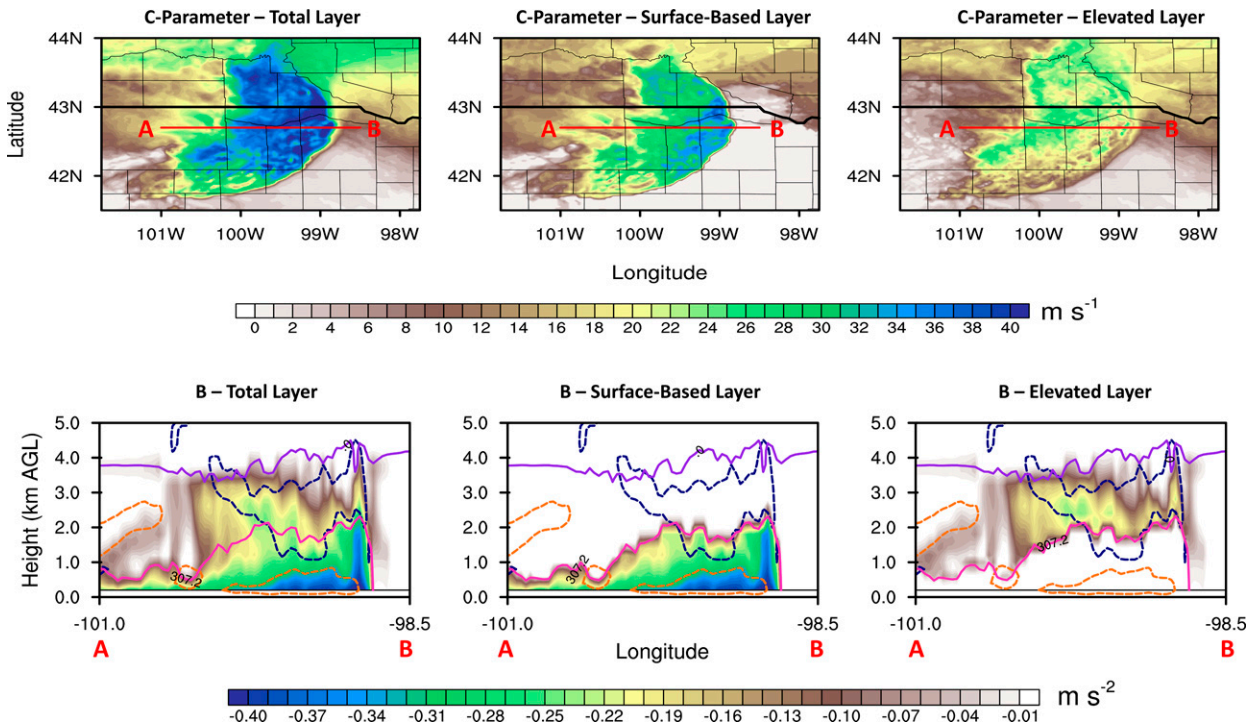
FIG. 4. Panel plot exemplifying the division of the MCS cold pool into vertical layers for the simulated 7 Jul 2016 case at 0000 UTC, just south of the Nebraska–South Dakota border. The grid spacing shown is 1 km–100 lev, employing WSM6 MP. Filled contours in the top plots represent the cold pool parameter $C$ (m s$^{-1}$) before any filtering was applied. The red line bisecting the $C$ values defines the cross sections in the bottom plots, with the cross-section end points labeled "A" and "B" in all plots. Negative buoyancy ($-B$; m s$^{-2}$) is shaded in the cross sections. The purple line is the freezing level. The pink line separating the surface-based and elevated-layer cold pools is $\overline{\theta}^{*}$, the averaged ambient surface potential temperature preceding the MCS. Positive horizontal vorticity exceeding $2 \times 10^{-2}$ s$^{-1}$ is shown via dark blue dashed lines, and orange dashed lines show $2 \times 10^{-2}$ s$^{-1}$ or greater magnitudes of negative vorticity, with a 9-point smoother applied to the contours with one pass to reduce noise. (left) The total cold pool, (center) the surface-based layer cold pool, and (right) the elevated-layer cold pool.

ratios, respectively. Like Squitieri and Gallus (2020), only $-B$ values below the freezing level were included in this study to extract $-B$ values associated with the cold pool. Multiple research tasks in this manuscript were repeated with a version of (2) that subtracted graupel and snow mixing ratios ($q_g$ and $q_s$ in kg kg$^{-1}$), with little to no change in the results noted given that most snow and graupel existed above the freezing level, hence the use of (2) in current form.

Unlike Squitieri and Gallus (2020), the $-B$ values contributing to MCS forward speeds were separated from the melting layer. The first layer is the lower-most portion of the cold pool with the highest concentration of $-B$, serving as the primary contributor to MCS forward speed (hereafter "surface-based layer"). The second layer of the cold pool resides above the surface-based layer and consists of a negatively buoyant layer of air which supports cold pool intensity mainly due to frozen hydrometeor melting aloft (hereafter called the "elevated layer"), as shown in Fig. 4. Similar to Parker et al. (2020) and Parker (2021), the surface-based layer is defined as the depth of potential temperatures less than the surface potential temperature immediately ahead of the MCS ($\overline{\theta}^{*}$). Conceptually, this represents the air ahead of the MCS which is lifted overhead by a leading-line low-level circulation driven

by the cold pool's forward motion. As such, surface-based layer cold pool depths at each grid point were defined by the height (m AGL) of $\overline{\theta}^{*}$. The total cold pool encompasses all integrated negative buoyancy up to and beneath the freezing level (Fig. 4, left column). The cold pool in the surface-based layer (Fig. 4, middle column) is restricted to $-B$ beneath $\overline{\theta}^{*}$, as in Parker (2021), and $-B$ in the elevated layer is confined between $\overline{\theta}^{*}$ and the freezing level (Fig. 4, right column). The depth of the cold pool elevated layer at each grid point was defined as the depth (m AGL) of $-B$ between $\overline{\theta}^{*}$ and where $-B = 0$ m s$^{-2}$ or the freezing level, whichever was first in elevation.

Cross sections of negative buoyancy overlaid with horizontal vorticity were analyzed for all cases, grid spacing, and MP configurations to confirm that the surface-based cold pool induced rising motion. Horizontal vorticity ($\eta$) was calculated as

$$\eta = \left(\frac{\partial w}{\partial y} - \frac{\partial v}{\partial z}\right)i + \left(\frac{\partial u}{\partial z} - \frac{\partial w}{\partial x}\right)j, \qquad (3)$$

where $u$, $v$, and $w$ are the east–west, north–south, and vertical wind components, respectively. The terms $i$ and $j$ represent
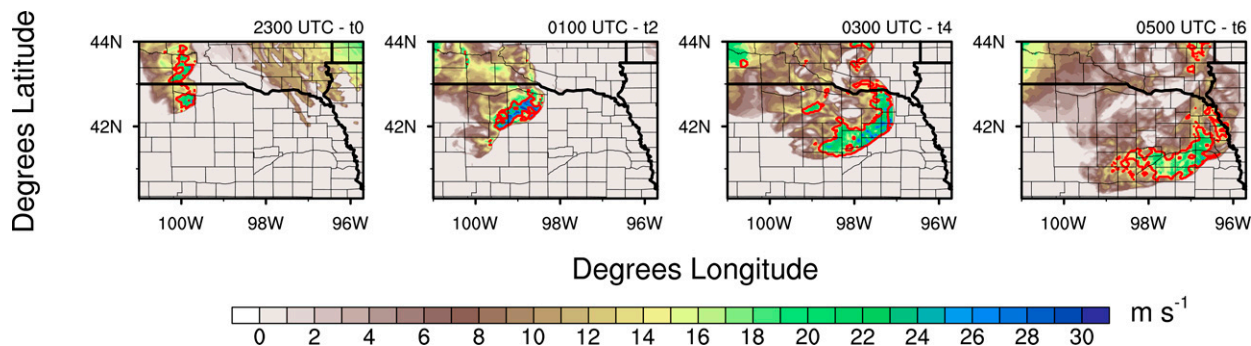
FIG. 5. Panel plot showing the evolution of the simulated 2 Jun 2018 MCS along the Nebraska–South Dakota border via unfiltered $C_{sl}$ magnitudes (shaded; m s$^{-1}$), starting at MCS initiation time (t0—2300 UTC for this case) and progressing at 2-h intervals, to t6—0500 UTC. The 3 km–50 lev grid spacing with Thompson MP is shown. The red lined contours in all plots represent $C_{sl}$ magnitudes after the dB$Z$ filter was applied, for all values exceeding the 75th percentile. The percentile values were derived via the intensity-weighted areal coverage method.

the west–east and north–south components of horizontal vorticity (Markowski and Richardson 2010). Negative buoyancy collocated with negative horizontal vorticity beneath $\overline{\theta}^{*}$ (exemplified in Fig. 4) is assumed to contribute to the outward-spreading portion of the gust front rotor noted in past studies (Droegemeier and Wilhelmson 1987; Dudhia et al. 1987), with positive vorticity occurring in the elevated cold pool layer. In addition, this horizontal vorticity configuration is consistent with rearward mass advection in the layer centered on the transition between negative and positive horizontal vorticity, affirming the use of $\overline{\theta}^{*}$ to vertically divide the cold pool between the surface-based and elevated layers. The cold pool was split in this manner to infer how differences in microphysical tendency behaviors (by melting near the freezing level or melting/evaporation closer to the surface) with changing $\Delta x$ and $\Delta z$ might influence cold pool intensity, by either strengthening or deepening the cold pool in the surface-based or the elevated layer.

Henceforth, cold pool parameter values in the surface-based layer or elevated layer will be referred to as $C_{sl}$ and $C_{elv}$ (respectively), with cold pool depths abbreviated in the same manner ($D_{sl}$ and $D_{elv}$). The cold pool parameter integrating buoyancy through the entire post-convective stable layer (surface-based layer + elevated layer) was also calculated and is referred to as $C_{total}$. Surface negative perturbation potential temperature absolute magnitudes ($\theta'_{sfc}$) were also evaluated to assess surface cold pool intensity.

### d. Calculation and aggregation of bulk statistics

For all research tasks performed in this study, WRF output was regridded to the coarsest grid spacing for fair comparison. First, all 1-km output were horizontally regridded to 3 km. Next, the 3- and (horizontally regridded) 1-km output on both 50 and 100 vertical levels was vertically regridded to a new 50 vertical levels stretched grid (in m AGL) that roughly corresponded to $\Delta z$ on the original 50 vertical levels grid. For each case, for each grid-spacing configuration, magnitude and areal or volumetric coverage (gridpoint count) bulk statistics were generated for all cold pool variables, as well as hydrometeor,

microphysical tendency, and other related variables to statistically analyze how model grid spacing changes effected MCS cold pool evolution. All 2D and 3D variables were averaged to a single value to represent MCS behavior, for each time $t$, starting at $t-3$ (3 h before simulated MCS initiation time) to t7 (7 h after simulated MCS initiation) in the following manner. First, all non-MCS related values (on a plane for 2D variables or in a column for 3D), were excluded where composite reflectivity was less than 35 dB$Z$. For the composite reflectivity, values at three times ($t-1, t, t+1$) were examined and summed together to account for a variable collocated with the MCS trailing precipitation region, or with the gust front potentially preceding storm cores.

For calculating single-value bulk statistics (surface area for 2D variables or gridpoint count for 3D), all reflectivity-filtered values of a given variable for all grid spacings were binned into a 1D array (sorted in ascending order) from which the 75th percentile was calculated (as shown for an example case using $C_{sl}$; Fig. 5). This 75th percentile value for all grid spacings of a variable was then applied to each grid-spacing configuration, where all values below this threshold were filtered out. The remaining values (the 75th percentile to the maximum value) were then averaged to a single value (bulk statistic). Bulk statistics were calculated this way to allow the grid-spacing configuration with greater coverage of higher values among a distribution of all possible values to carry greater weight (and is hereafter referred to as "intensity weighted"). Though arbitrary, the 75th percentile was chosen to sample the stronger portions of the cold pool and associated processes contributing to cold pool evolution. Finally, before statistics were aggregated among cases, data depicted in time series were temporally averaged (data at the current time plus the previous and future hour divided by 3) to smooth out irregularities in the aggregated results potentially introduced by a small sample size.

Given the limited sample size of 11 cases, bootstrap statistical significance testing was performed on the bulk statistics with a two-tailed hypothesis-based $t$ test provided in Mendenhall and Sinich (2007), with resampling performed 10 000 times (as in Squitieri and Gallus 2020) whenever quantitative

TABLE 3. Six unique model grid-spacing pairs on which bootstrap statistical significance tests were performed using the two-tailed method are shown.

| Bootstrap statistical significance comparisons | | |
|---|---|---|
| Sample A | | Sample B |
| 3 km–50 lev | ← → | 3 km–100 lev |
| 3 km–50 lev | ← → | 1 km–50 lev |
| 3 km–50 lev | ← → | 1 km–100 lev |
| 3 km–100 lev | ← → | 1 km–50 lev |
| 3 km–100 lev | ← → | 1 km–100 lev |
| 1 km–50 lev | ← → | 1 km–100 lev |

comparisons between runs with varying $\Delta x$ or $\Delta z$ were made. Since two-tailed hypothesis testing was applied, only six unique pairs of model $\Delta x$ and $\Delta z$ comparisons were necessary (and are shown in Table 3). Significance was achieved when a $p$ value of 0.05 or lower was realized, with confidence in rejecting the null-hypothesis exceeding 95%. If the $p$ value fell between 0.05 and 0.10 (90th–95th confidence interval), the difference between two compared samples was considered "statistically noticeable."

### e. Using MODE to count updrafts with runs varying model grid spacing

The Method for Object-Based Diagnostic Evaluation tool (MODE; Davis et al. 2006a,b) was employed to count the number of updrafts which comprised organized deep convection across the 1-km domain and the area of the 3-km parent domain comprising the area covered by the 1-km nest. 2D updraft fields were calculated at each model grid point by determining the maximum value of positive vertical velocity ($w$) within a prescribed depth of the troposphere. Updrafts for all grid spacings of simulations were split between the low levels (1–4 km AGL maximum values) and midlevels (at or above 5 km AGL, noted as 5+ km AGL henceforth) to differentiate the contributions made by low- and midlevel updrafts after $w$ was horizontally and vertically regridded to the coarsest grid. Since updrafts tended to slope with height in the low levels, the more discrete midlevel updrafts were counted by MODE via the 2D composite 5+ km AGL $w$ field. To be able to count the smallest of updrafts contributing to leading-line MCS evolution, no convolution or area thresholds were applied to the 2D fields, though updrafts required 15 m s$^{-1}$ minimum intensities to be counted.
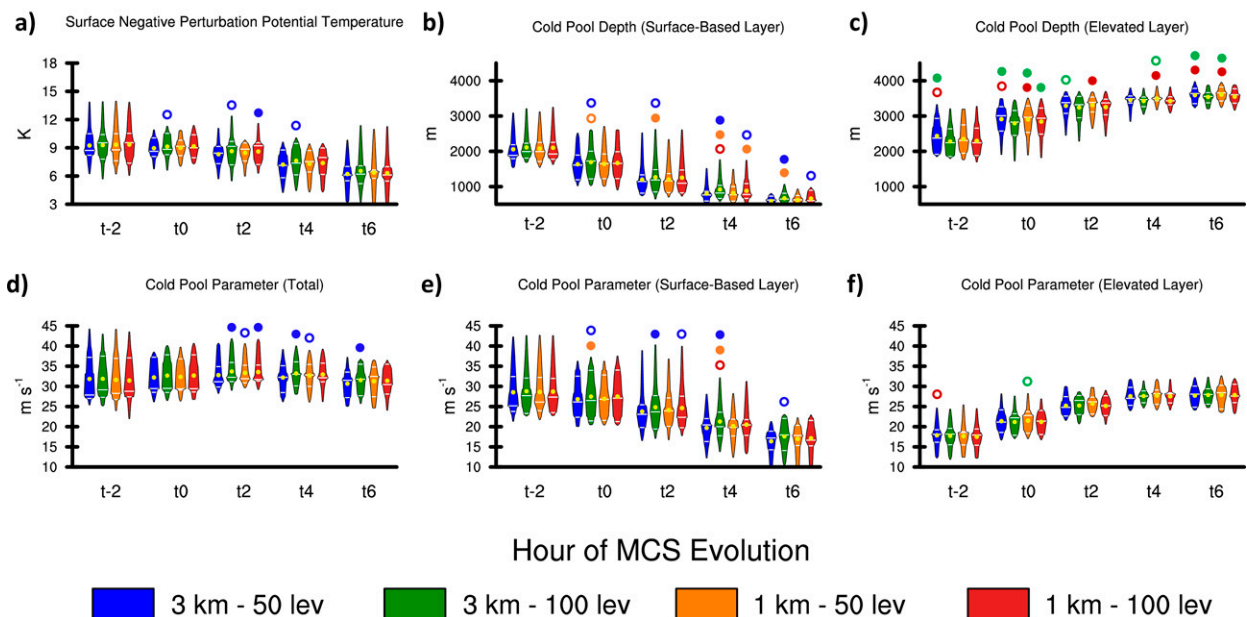


FIG. 6. Violin plots showing the distribution of averaged magnitudes exceeding the 75th percentile among 11 cases for (a) $\theta'_{sfc}$ (K), (b) $D_{sl}$ (m), (c) $D_{elv}$ (m), (d) $C_{total}$ (m s$^{-1}$), (e) $C_{sl}$ (m s$^{-1}$), and (f) $C_{elv}$ (m s$^{-1}$). Distributions were calculated for every 2 h of MCS evolution (from 2 h before to 6 h after MCS structure is achieved) for 3 km–50 lev (blue), 3 km–100 lev (green), 1 km–50 lev (orange), and 1 km–100 lev (red). White horizontal lines on the violins delineate the 25th, 50th, and 75th percentiles. Bootstrap statistical significance testing was done between all grid-spacing pairs at each hour, for each variable, where statistical significance is achieved with a $p$ value at or less than 0.05. Filled dots indicate where a sample is statistically significantly larger than the sample represented by the color of the dot. For example, at t4 for $D_{sl}$ in (b), 3 km–100 lev (green violin) cold pools are significantly deeper than 1 km–50 lev (orange filled dot) and 3 km–50 lev (blue filled dot). Hollow dots represent the same testing philosophy as the filled dots, but for $p$ values between 0.05 and 0.10, and are considered statistically noticeable.

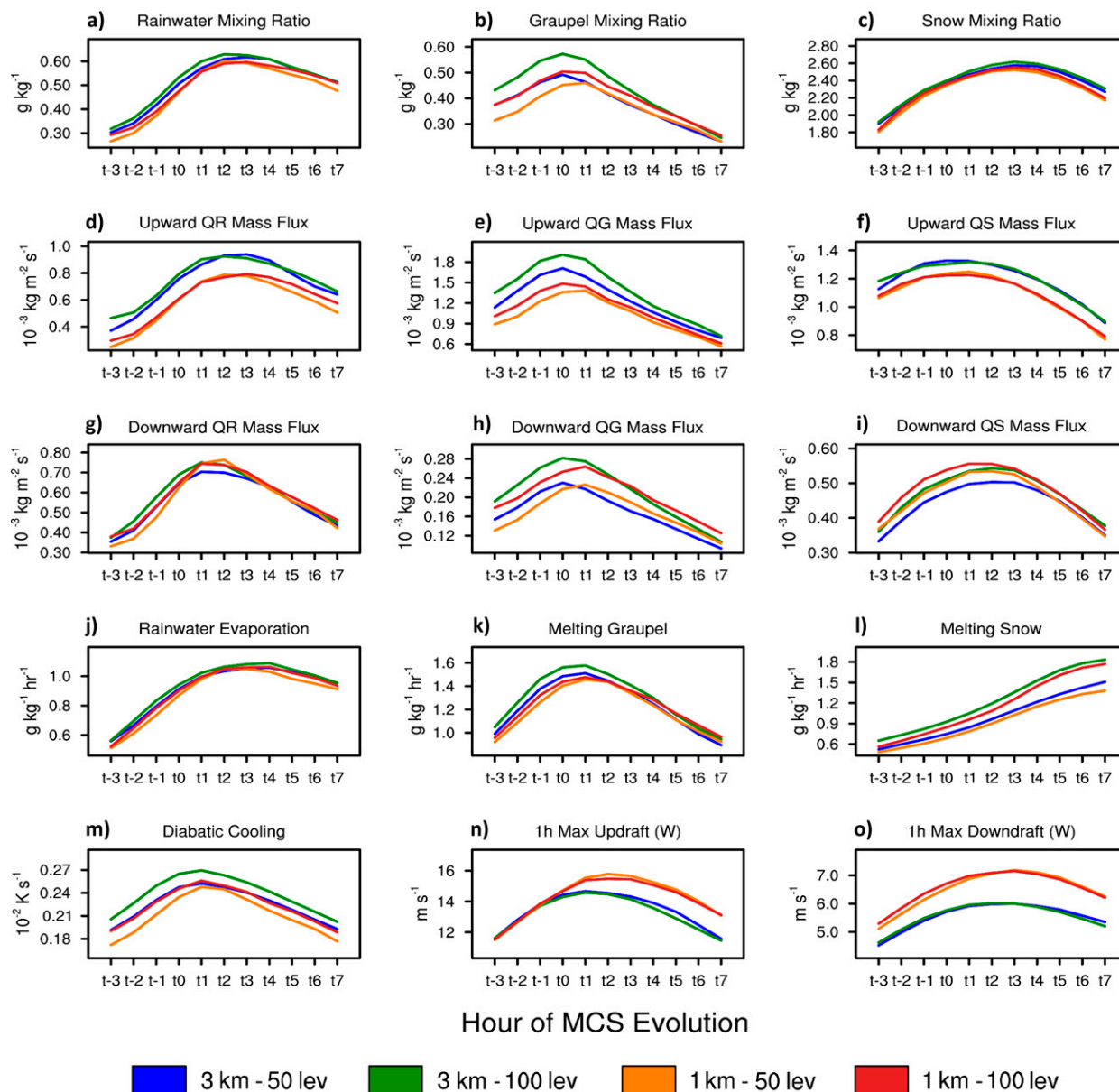## Thompson Scheme - 75th Percentile



FIG. 7. Time vs magnitude plots showing absolute value bulk magnitudes averaged above the 75th percentile for all 11 cases, calculated for each hour of MCS evolution (from 3 h before to 7 h after MCS structure is achieved) for 3 km–50 lev (blue), 3 km–100 lev (green), 1 km–50 lev (orange), and 1 km–100 lev (red) WRF Thompson MP runs. The variables depicted are (a)–(c) rainwater, graupel and snow mixing ratios; (d)–(f) upward mass fluxes of the aforementioned hydrometeors; (g)–(i) as in (d)–(f), but for downward mass fluxes; (j) production of water vapor by evaporating rainwater; (k) production of rainwater by melting graupel; (l) production of rainwater by melting snow; (m) total microphysical latent cooling below the freezing level; (n) 1-h accumulated maximum updraft velocities; (o) as in (n), but for downdrafts.

## 3. Results

### a. Statistical differences in cold pool intensities through MCS evolution

For aggregated bulk statistics for 2D cold pool fields in Thompson MP runs, surface cold pools (Fig. 6a) were very similar in magnitude, with the average absolute value of $\theta'_{\text{sfc}}$

for all 11 cases hovering around 9 K through much of the MCS's life cycle, though 3 km–100 lev surface cold pools were statistically noticeably colder during and after MCS initiation (t0–t4). Similar magnitudes of $C_{\text{total}}$ were also shared among the varying grid spacings preceding MCS initiation and throughout MCS evolution (Fig. 6d). When considering only magnitudes, cold pools with coarser grid spacing were slightly more
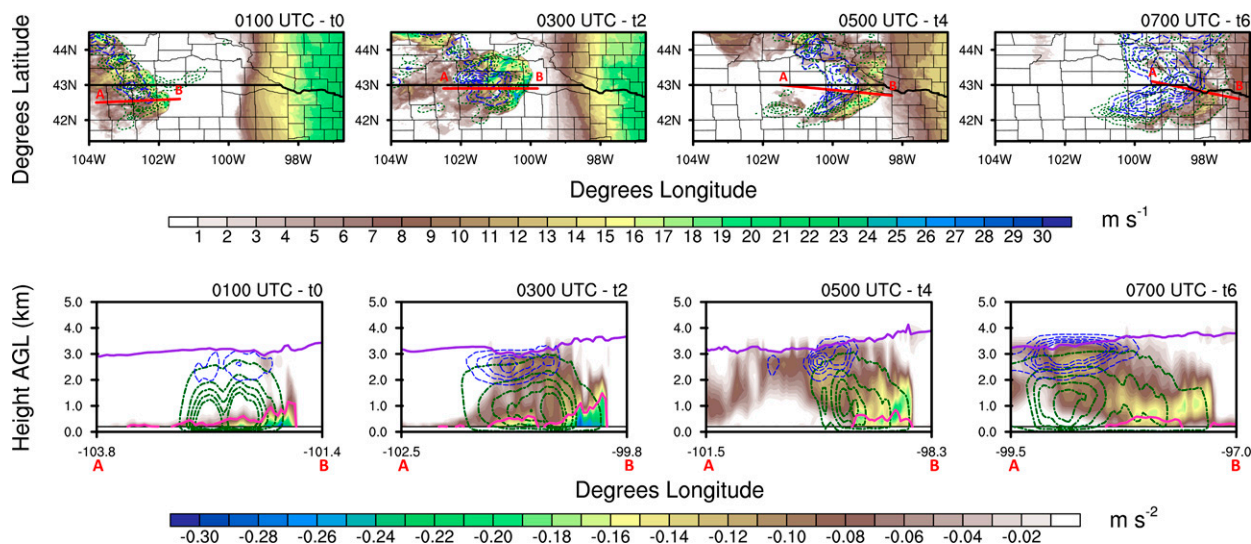
FIG. 8. (top) Planar panels depicting the evolution of the simulated 3 Jun 2015 MCS that traversed the South Dakota–Nebraska border using the 1 km–100 lev grid spacing and Thompson MP. (bottom) The cold pool via $C_{sl}$, unfiltered (filled contours; m s$^{-1}$) and dashed-lined contours representing composite values of production of water vapor by evaporating rainwater (green, from 0 to 2.5 at intervals of 0.5 g kg$^{-1}$ h$^{-1}$) and production of rainwater by melting snow (blue, from 1 to 10 at intervals of 2 g kg$^{-1}$ h$^{-1}$), overlaid by a red line depicting cross sections. "A" and "B" delineate the start and end points of the cross section. Filled contours in the cross section are negative buoyancy ($-B$; m s$^{-2}$), with the pink line representing $\overline{\theta}^{*}$ splitting the cold pool between the surface-based and elevated layers. The dark purple line denotes the freezing level. Production of water vapor by evaporating rainwater is shown by dashed green lines (0–2.5 at intervals of 0.5 g kg$^{-1}$ h$^{-1}$), with blue dashed lines being production of rainwater by melting snow (0–5 at intervals of 1 g kg$^{-1}$ h$^{-1}$).

intense than cold pools with finer grid spacing. The $C_{total}$ intensity differences between $\Delta x = 3$- and 1-km simulated cold pools were not overall statistically significant (similar to Squitieri and Gallus 2020), though 3-km (and occasionally 1-km) simulations with 100 vertical levels cold pools were significantly stronger than those employing 50 vertical levels, suggesting that some sensitivity exists to decreasing $\Delta z$.

When dividing Thompson MP cold pools into surface-based and elevated layers, depth and intensity trends among all configurations, as well as more significant differences in cold pool attributes between $\Delta x$ and $\Delta z$ became apparent. First, a gradual decline in $D_{sl}$ and $C_{sl}$ magnitudes was noted among all grid spacings (Figs. 6b,e) as $D_{elv}$ and $C_{elv}$ magnitudes increased when advancing through the MCS life cycle (Figs. 6c,f). Greater $-B$ intensities and depths likely shifted from the surface-based to elevated layer in all grid spacings due to the perseverance of rainwater evaporation (Fig. 7j) combined with the continuous increases of melting snow (also noted in Bao et al. 2019 and shown in Fig. 7l), contributing to more negative buoyancy in the elevated layer from t3 onward in MCS evolution. Past studies have noted that frozen hydrometeors (including snow) are advected upward and rearward to the trailing precipitation region of the MCS by a secondary upper-level vertical circulation consisting of slantwise convection (Rutledge and Houze 1987; Fovell and Ogura 1988). As seen in all 11 simulated cases and exemplified in the 03 June 2015 case (Fig. 8), trailing regions of melting snow from rearward advected frozen hydrometeors atop a deep layer of evaporating rain would generate modest but deeper layers of $-B$ through MCS evolution. Deeper $-B$ would extend well behind the convective leading line (as in

Caniaux et al. 1994; Gallus and Johnson 1995b) through the elevated layer as the surface-based layer diminished (seen by the decreasing depths of $\overline{\theta}^{*}$; Fig. 8, bottom row). This trailing $-B$ originating from the trailing precipitation region comprising $C_{elv}$ contributes up to 20 m s$^{-1}$ of integrated negative buoyancy (similar to what is shown in Fig. 4), as also inferred by past studies (Lafore and Moncrieff 1989; Parker et al. 2020).

The 3 km–100 lev and 1 km–100 lev $D_{sl}$ was statistically noticeably to significantly deeper (Fig. 6b), with $C_{sl}$ stronger (Fig. 6e) than 50 vertical levels runs around MCS t0 and within the first few hours of the MCS life cycle, with 3 km–100 lev $C_{sl}$ remaining statistically noticeably to significantly stronger than 50 vertical levels runs through the remainder of MCS evolution. Past research has shown that rainfall evaporation is the primary contributor to cold pool intensity (Fujita 1959; Mallinson and Lasher-Trapp 2019). In the present work, similar rainfall evaporation rates as well as rainwater mixing ratios and associated downward fluxes were noted among all grid-spacing configurations, though 3-km simulated MCSs did exhibit stronger upward mass fluxes throughout their life cycle (Figs. 7a,d,g,j). However, ice-based processes appeared to be the primary contributor to changes in cold pool attributes and evolution with $\Delta x$ and $\Delta z$ decreases. The evaluation of microphysical tendencies shows that the 3-km graupel mixing ratios, upward and downward fluxes, melting graupel rates, and diabatic cooling rates below the freezing level appear to be greater than those in the 1-km runs, leading up to MCS initiation and for a few of hours afterward (Figs. 7b,e,h,k,m). Later in simulated MCS evolution, higher graupel concentrations, downward fluxes of graupel and snow, and melting snow
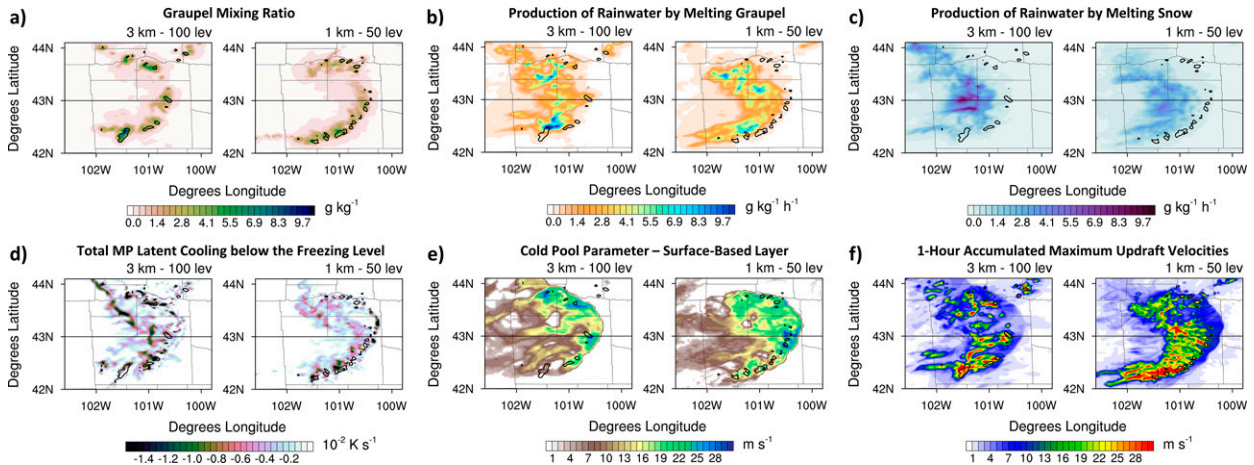
FIG. 9. Multipanel plot of the 3 Jun 2015 case at 0300 UTC, depicting filled contours of (a) graupel mixing ratio (g kg$^{-1}$), (b) production of rainwater by melting graupel (g kg$^{-1}$ h$^{-1}$), (c) production of rainwater by melting snow (g kg$^{-1}$ h$^{-1}$), (d) total microphysical latent cooling below the freezing level (10$^{-2}$ K s$^{-1}$), (e) $C_{sl}$ (m s$^{-1}$), and (f) 1-h accumulated maximum updraft velocities (m s$^{-1}$). The 2D graupel mixing ratio, melting graupel and snow rates, and microphysical cooling rates shown are composite values, with the maximum value in a vertical column selected for plotting. Black lined contours denote composite vertical velocities, where deep convective updraft intensities reached or exceeded 15 m s$^{-1}$. The 3 km–100 lev, and 1 km–50 lev simulations are shown at left and right, respectively, in each panel set.

rates occurred with 3 km–100 lev and 1 km–100 lev runs (Figs. 7b,h,i,l).

In 100 vertical levels simulations, stronger downward fluxes of higher graupel concentrations toward the freezing level likely supported greater melting graupel rates near the leading line, as shown in an example case (Figs. 9a,b) and noted in nearly all

other cases. Combined with greater snow melting rates farther back from the leading line (Fig. 9c), greater total microphysical cooling manifested below the freezing level in 100 vertical levels runs (Fig. 9d). In turn, greater $-B$ developed in the melting layer, which descended closer to the surface to support stronger 1 km–100 lev and especially 3 km–100 lev $C_{sl}$, with significantly
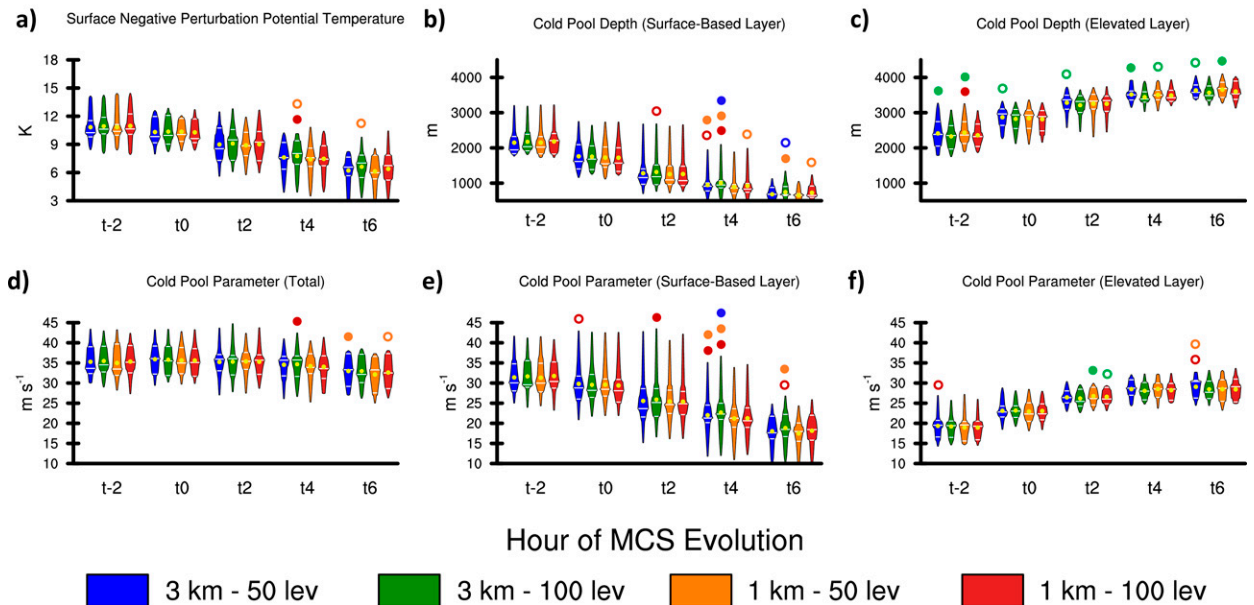


FIG. 10. As in Fig. 6, but for WSM6 MP runs.
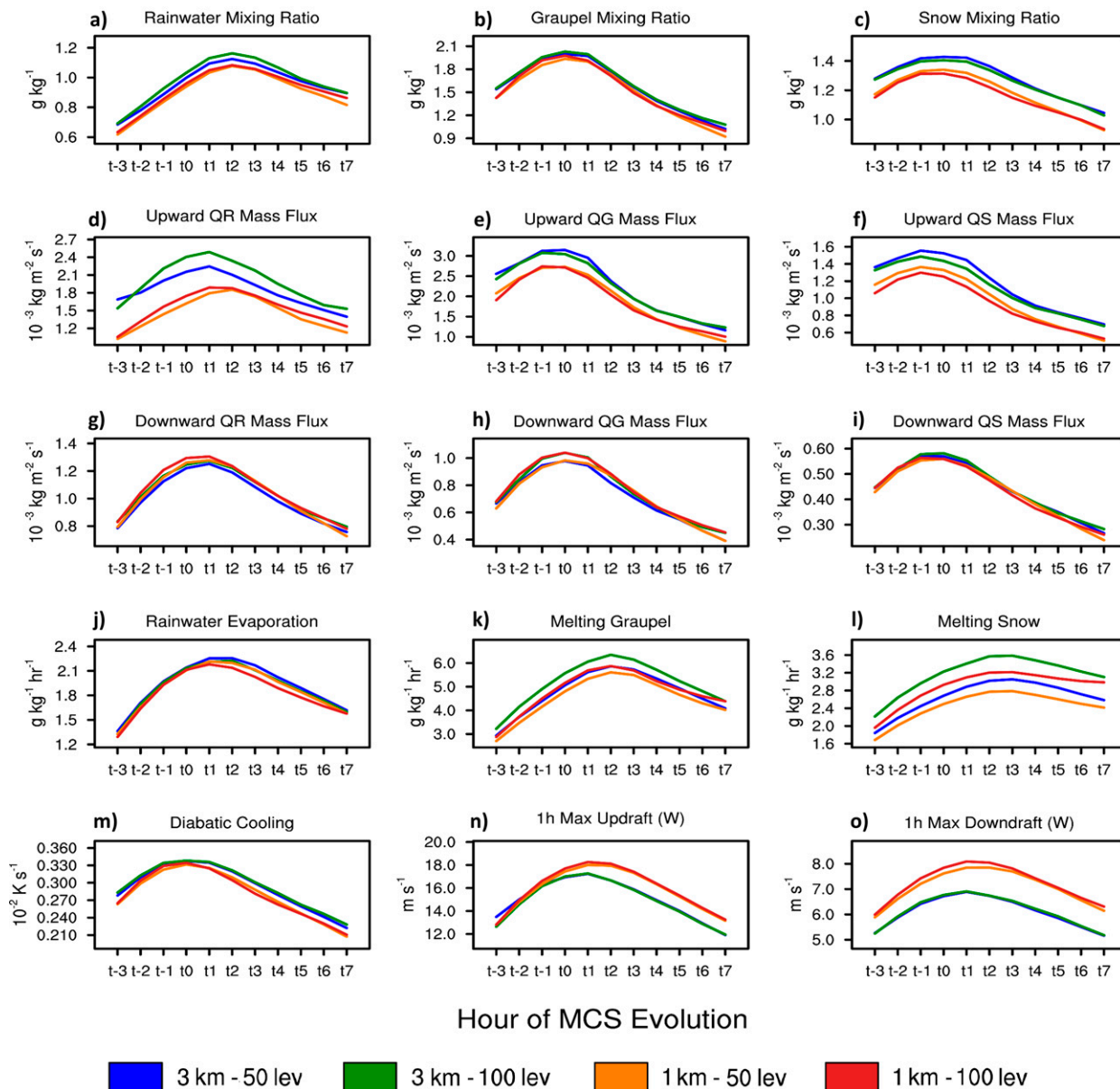
## WSM6 Scheme - 75th Percentile



FIG. 11. As in Fig. 7, but for WSM6 MP runs.

shallower and weaker 1 km–100 lev and 3 km–100 lev $D_{elv}$ relative to 50 vertical levels, especially early in MCS evolution (Figs. 6c,f). As noted in previous studies, graupel would develop within the trailing precipitation region from snow (Rutledge 1986) and descend to the melting layer, contributing to downward momentum transport via a lower-level secondary vertical circulation (Gallus and Johnson 1995b) and becoming a major contributor to latent cooling (as in Grim et al. 2009). Figures 7j–k, as well as past research (Leary and Houze 1979) shows that melting graupel and rainwater evaporation can occur with similar magnitudes, inferring that graupel melting can play a similarly important role as rainwater

evaporation when contributing to cold pool development and intensity. Given the inherent "noisy" output of updrafts, hydrometeor concentrations and tendencies, and latent cooling fields (Figs. 9a–d), it was extremely difficult to derive meaningful cross-sections that would explicitly show how graupel concentrations, fluxes, melting rates, and total microphysical latent cooling magnitudes directly descended through the column and impacted $-B$ with decreased $\Delta x$ and $\Delta z$. This was the primary reason for aggregating bulk statistical results among the 11 simulated cases to determine the causes of cold pool evolution changes with decreased $\Delta x$ and $\Delta z$.
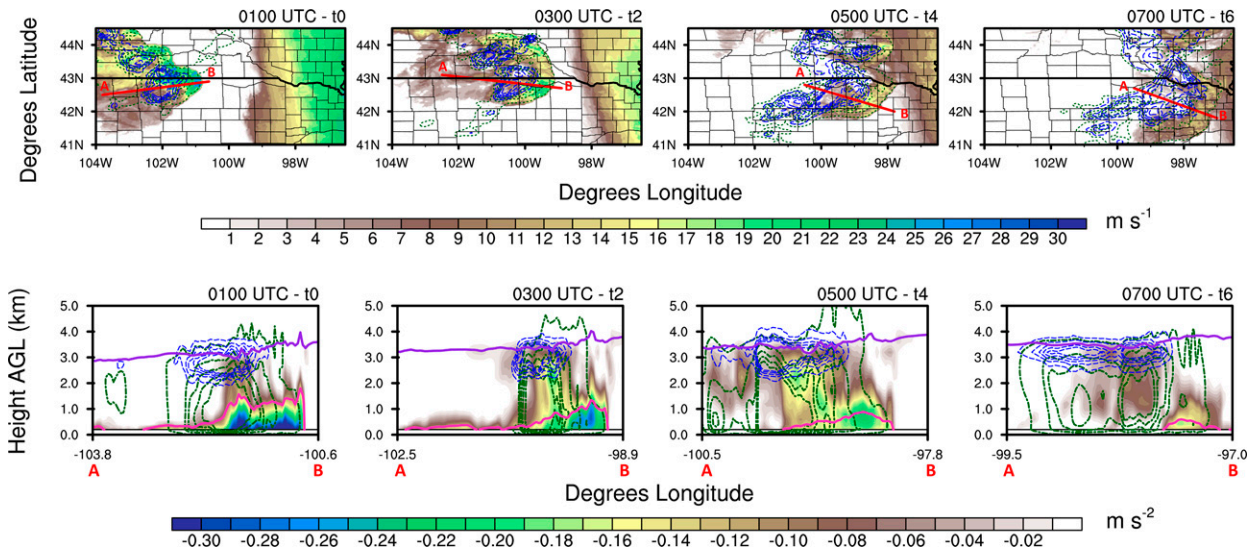
FIG. 12. As in Fig. 8, but for the WSM6 MP scheme.

Hirt et al. (2020) noted that finer $\Delta x$ simulations of deep convection produced less leading-line total mass flux. The greater upward and downward mass fluxes of larger rainwater, graupel, and snow concentrations (Fig. 7d–f) in the coarser 3-km runs were likely caused by weaker (Figs. 7n–o) but larger (lesser-resolved) updrafts and downdrafts with greater upward and downward mass fluxes which in turn supported relatively higher melting graupel and total microphysical latent cooling rates relative to 1-km runs. Figure 9 depicts a classic case where updraft intensities were overall weaker in 3-km runs compared to 1 km (Fig. 9f), but the updraft sizes

were larger (especially for 3 km–100 lev runs, Fig. 9—black lined contours in any plot). In the example case at 0300 UTC, stronger $C$ magnitudes of the 100 vertical levels surface-based layer cold pools ($C_{sl}$) were concentrated on the northern and southeastern cold pool bounds (Fig. 9e), where some of the larger updrafts and associated highest graupel mixing ratios, melting graupel rates, and total latent microphysical cooling occurred (Figs. 9a–d). With finer vertical grid spacing employed in the melting layer, melting graupel and snow from slow-falling smaller graupel species (noted with Thompson MP performance in Bao et al. 2019) and rainwater evaporation rates
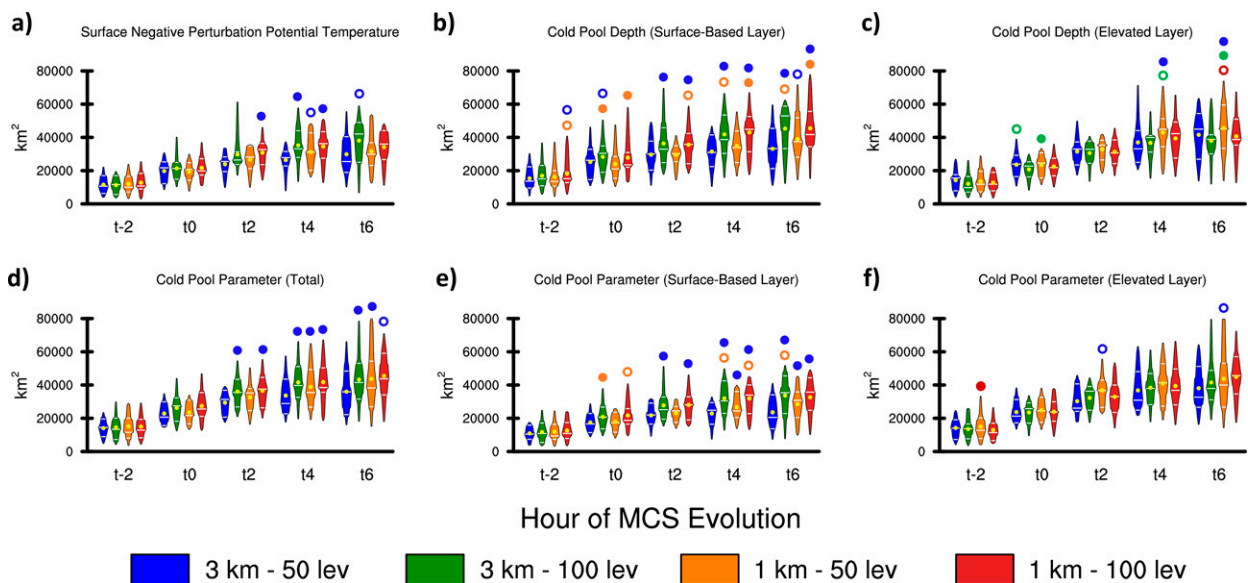


FIG. 13. As in Fig. 6, but for intensity-weighted areal coverage (km$^2$) exceeding the 75th percentile.
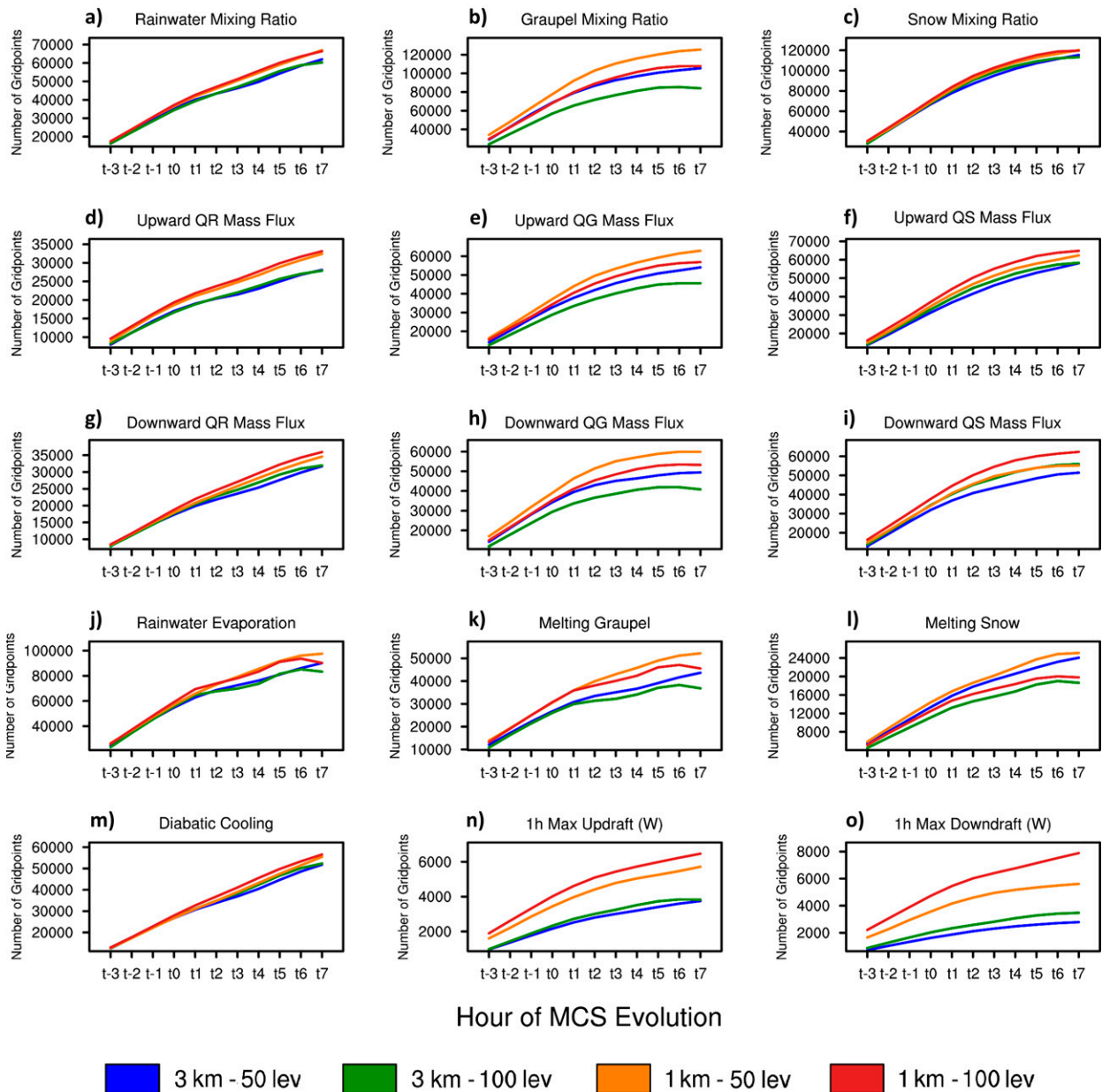
## Thompson Scheme - 75th Percentile



FIG. 14. As in Fig. 7, but for intensity-weighted coverage (in number of grid points) exceeding the 75th percentile in Thompson MP simulations. The hydrometeor concentrations, fluxes, and tendency coverages are three-dimensional throughout the MCS and are considered volumetric in (a)–(m), while the 1-h maximum accumulated updraft and downdraft fields are 2D, with the number of grid points comprising an areal coverage.

may also be better resolved relative to coarser $\Delta z$ runs. Better vertically resolved frozen hydrometeor processes combined with the impacts of under-resolved updrafts with greater mass fluxes and generation of hydrometeors to melt and evaporate may explain why the 3 km–100 lev $C_{sl}$ magnitudes were strongest and the $D_{sl}$ depths greatest in this experiment.

Many of the cold pool evolutionary trends common among all grid spacings in Thompson MP simulations were also present in WSM6 MP runs. Among all grid spacings, $D_{sl}$ became shallower with time (Fig. 10b) and $C_{sl}$ gradually weakened (Fig. 10e), as $D_{elv}$ and $C_{elv}$ magnitudes increased through MCS evolution (Figs. 10c,f).

As in the Thompson MP simulations, the increase or persistence in rainfall evaporation, melting graupel, and melting snow rates among all 11 cases (Figs. 11j–l) likely contributed to the increasing depth of the cold pool into the elevated
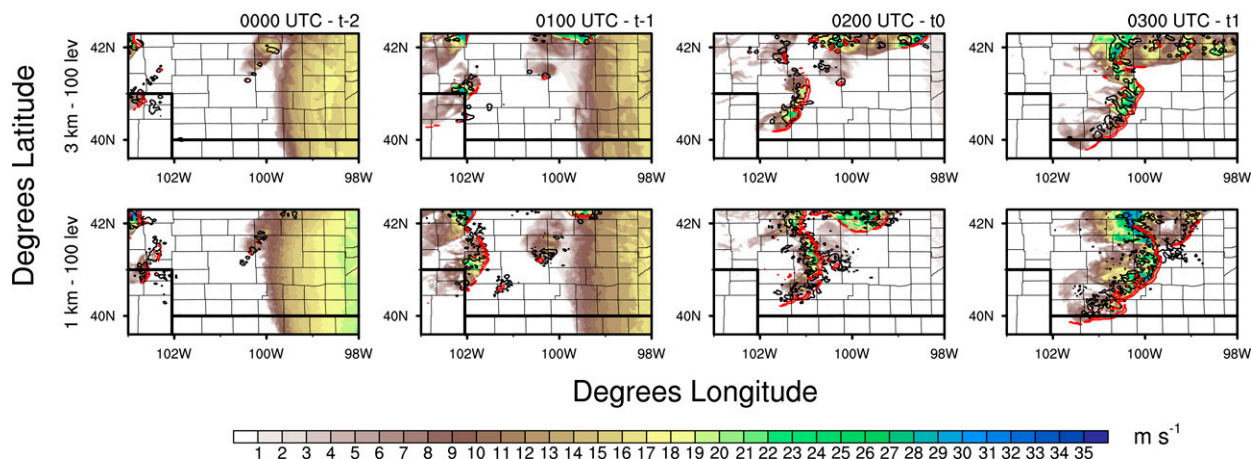
FIG. 15. Progression of the 9 Jul 2020 MCS surface-based cold pool (unfiltered $C_{sl}$, filled contours; m s$^{-1}$) from the onset of MCS initiation to the early stages of MCS growth ($t − 2$ to t1, shown from left to right), for the (top) 3 km–100 lev and (bottom) 1 km–100 lev Thompson MP simulations. Black lined contours depict 5+ km AGL (midlevel) updrafts, with red lined contours representing 1–4 km AGL (low-level) updrafts, both exceeding 5 m s$^{-1}$. While the updraft count threshold in MODE was 15 m s$^{-1}$ for the 5+ km AGL updrafts, 5 m s$^{-1}$ threshold updrafts were shown here for better visibility of the more widespread midlevel updraft coverage.

layer, with trailing melting snow and evaporating rain contributing to the cold pool width through MCS evolution (shown again with the 3 June 2015 case; Fig. 12, but with WSM6 MP). Like Thompson MP, 3 km–100 lev $C_{sl}$ and $D_{sl}$ were significantly stronger and deeper compared to 1 km–50 lev (Figs. 10b,e), though this trend was mainly evident later in MCS evolution (t4–t6). Unlike Thompson MP, only 3 km–100 lev $D_{elv}$ was significantly shallower compared to 50 vertical levels simulations (Figs. 10c,f). Moreso, WSM6 MP based 3 km–100 lev $C_{sl}$ and $D_{sl}$ were noticeably to significantly greater than 1 km–100 lev through the MCS cycle, which was not as prevalent in Thompson MP runs. Also, when evaluating, $D_{sl}$, or $C_{sl}$ (Figs. 10b,e), 3 km–100 lev cold pools (and to an extent 3 km–50 lev) were significantly deeper and stronger than their 1-km counterparts, especially at t4.

Like Thompson MP, rainwater evaporation rates were of similar magnitudes among grid spacings through MCS evolution (Fig. 11j). While graupel concentrations were very similar among the grid spacings (Fig. 11b), runs with coarser grid spacing were associated with higher rainwater and snow mixing ratios (Figs. 11a,c), with melting graupel and snow being the predominant tendencies contributing to latent cooling, which were highest in magnitudes for 3 km–100 lev runs (Figs. 11k–m). It is believed that cold pools with coarser grid spacing (especially with 100 vertical levels) depicted significantly deeper $D_{sl}$ and stronger $C_{sl}$ for the same reasons noted with Thompson MP simulations. Larger, (lesser resolved) and weaker updrafts and downdrafts (Figs. 11n,o) with greater upward and downward mass fluxes (Figs. 11d–f) in coarser $\Delta x$ runs supported rearward advection of higher concentrations of both liquid and ice hydrometeor species (per updraft) behind the MCS leading line, with greater rainwater and snow melting rates resolved with the 100 vertical levels grid spacing to support significantly stronger $C_{sl}$, deeper $D_{sl}$, and colder $\theta'_{sfc}$. Bao et al. (2019) noted that for WSM6 MP, graupel sizes are larger and tend to

exhibit greater fall speeds compared to Thompson MP. In the absence of stronger downward hydrometeor mass fluxes with runs employing coarser grid spacing (Figs. 11g–i), downward descending hydrometeors crossing the freezing level into a better resolved melting layer likely supported greater graupel and snow melting rates and subsequent higher rainwater mixing ratios in 3 km–100 lev WSM6 MP runs to generate much higher magnitudes of $C_{sl}$ and $D_{sl}$.

b. *Contribution of updraft coverage and intensity to MCS cold pool expanse*

The intensity-weighted areal coverage of Thompson MP simulated cold pools at the 75th percentile for all grid spacings increased through the stages of MCS evolution, regardless of the cold pool variable analyzed (Figs. 13a–f). Surface and total cold pool combined intensities and expanses in 1 km–50 lev and both 3 km–100 lev and 1 km–100 lev runs were noticeably to significantly larger than 3 km–50 lev runs from t2 onward (Figs. 13a,d). Splitting cold pools into surface-based and elevated layers shows that 3 km–100 lev and 1 km–100 lev $D_{sl}$ and $C_{sl}$ intensities and coverage were significantly greater than those in the 50 vertical levels runs through MCS evolution (Figs. 13b,e). In addition, 1 km–50 lev $D_{elv}$ and $C_{elv}$ were noticeably to significantly more expansive than all 3-km cold pools toward the later stages of MCS evolution (Figs. 13c,f).

These results suggest that grid spacing changes have the greatest impact on simulated MCS surface-based cold pool evolution. Corresponding with stronger, more expansive 1-km surface-based cold pools is greater volumetric coverage of rainwater, graupel, and snow mixing ratios and associated upward and downward fluxes exceeding the 75th percentile in 1- versus 3-km runs (Figs. 14a–i). Though the overall volumetric coverage of total microphysical cooling associated with Thompson MP runs only slightly increases when refining $\Delta x$ (Fig. 14m), the areal coverage of 1-h maximum accumulated
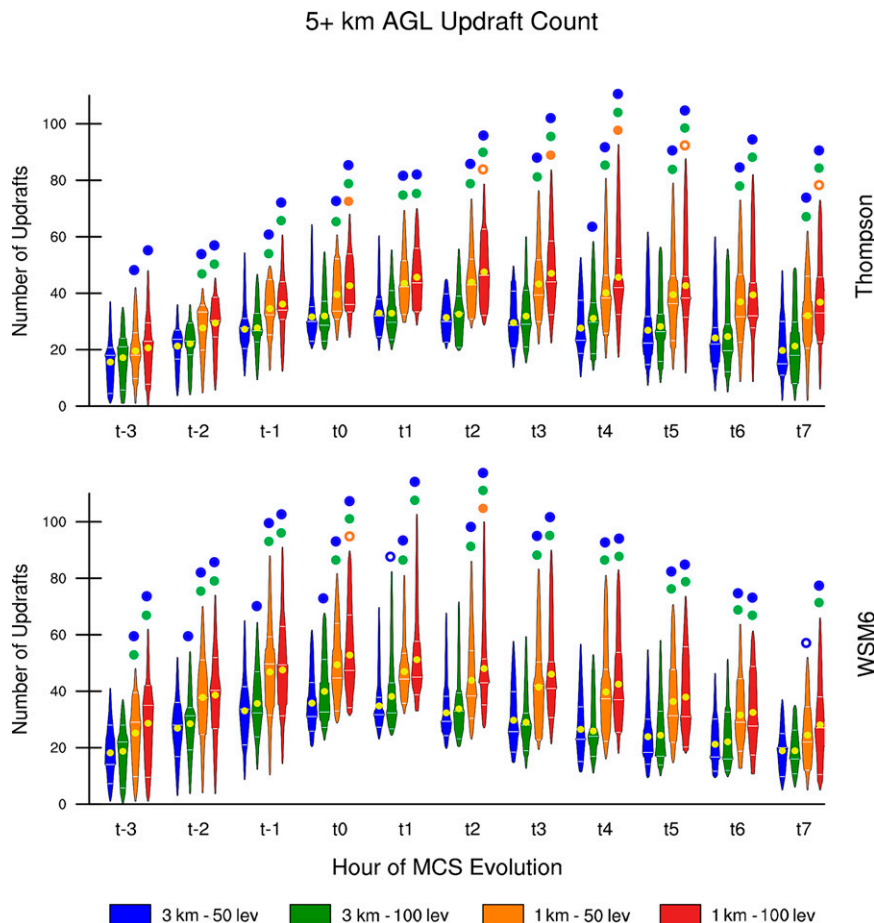
FIG. 16. Violin plot showing the number of MODE-derived objects in the 5+ km AGL (midlevel) positive $w$ field in aggregation of the 11 simulated cases, for each hour of MCS evolution, employing the (top) Thompson and (bottom) WSM6 MP schemes. Each object represents a midlevel updraft with 15 m s$^{-1}$ minimum threshold. The blue, green, orange, and red violins represent the distribution of updraft counts for the 3 km–50 lev, 3 km–100 lev, 1 km–50 lev, and 1 km–100 lev runs, respectively. White horizontal lines on the violins delineate the 25th, 50th, and 75th percentiles. Statistical significance is displayed as in Fig. 6.

updraft and downdraft intensities increase greatly (Figs. 14n–o). In turn, greater volumetric coverage of rainwater evaporation as well as melting graupel and snow occurs in 1-km simulations (Figs. 14j–l).

Positive vertical velocity fields were qualitatively and quantitatively evaluated to assess whether more abundant, intense updrafts were contributing to overall stronger, more expansive cold pools. When examining positive composite vertical velocity fields (maximum +$w$ grid point column value) in the 1–4 km AGL and 5+ km AGL layers (low-level and midlevel updrafts, respectively), it was found that deep convective leading lines consisted of more frequent, continuous 15+ m s$^{-1}$ midlevel updrafts as both $\Delta x$ and $\Delta z$ were decreased, roughly agreeing with Kain et al. (2008), who noted a greater coverage of individual storms when decreasing $\Delta x$ from 4 to 2 km. As exemplified in the 9 July 2020 case (Fig. 15, black lined contours) a greater number of midlevel updrafts encompass the pre-MCS convection in 1-km runs 1–2 h before MCS

initiation. The pre-MCS cold pool and low-level updraft coverage exceeding 5 m s$^{-1}$ (red lined contours) have similar areal coverage around $t - 2$. However, around $t - 1$ and t0, the greater areal coverage and spatial frequency of the more numerous midlevel updrafts along the MCS leading line in 1-km runs appear to correspond with a more expansive cold pool, also with greater low-level leading-line lift (evident via the longer red lines along the front edge of the cold pool). More frequent midlevel and low-level updrafts along the leading line of developing and maturing MCSs (as in Fig. 15) was qualitatively noted with the other 10 cases.

When evaluating aggregated midlevel updraft counts from the MODE derived statistics for all 11 cases (Fig. 16, top), the number of 15+ m s$^{-1}$ midlevel updrafts became statistically significantly greater when $\Delta x$ was decreased from 3 to 1 km, with 1 km–100 lev updrafts occasionally becoming statistically noticeably to significantly more frequent than 1 km–50 lev. It is likely that the stronger, better resolved low-level lift ahead
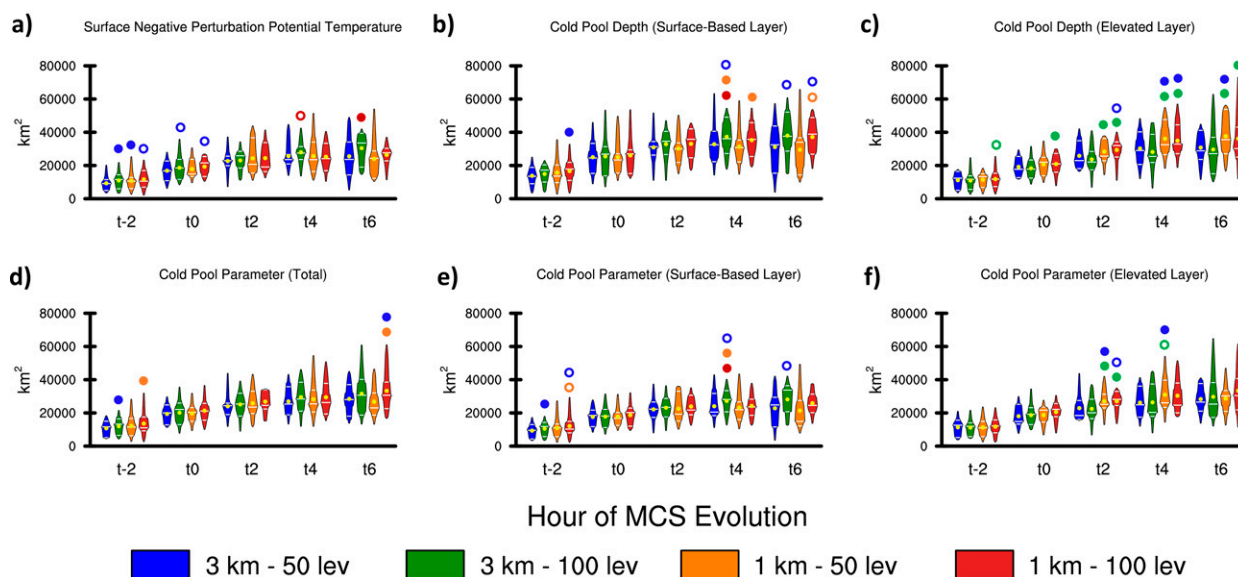
## WSM6 - Areal Coverage (75th Percentile)



FIG. 17. As in Fig. 13, but for WSM6 MP runs.

of the 1 km–100 lev cold pools triggered additional midlevel convective updrafts, hence why 1 km–50 lev runs had fewer midlevel updrafts than their 100 vertical levels counterparts.

The absolute magnitudes of cold pools and associated hydrometeor concentrations, fluxes and tendencies were typically higher in 3 km–100 lev runs than in the other grid spacings. However, greater expanses of stronger cold pool magnitudes and associated hydrometeor fluxes and tendencies were prevalent in the 1-km runs in tandem with the more frequent, intense updrafts, as in the single-case study by Fan et al. (2017) but reaffirmed with 11 simulated MCS cases in the present work. It is speculated that the more frequent, intense midlevel updrafts in 1-km runs fostered more expansive rearward advection of hydrometeors and associated latent cooling which supported stronger, more expansive $-B$ fields. A more expansive surface-based cold pool would emerge, encouraging greater low-level leading-line ascent within a thinner convective leading line. This stronger, more progressive leading line would support further cold pool expanse through the MCS life cycle, which may explain why the more expansive surface-based cold pools were associated with greater coverage of 1-km low-level AGL updrafts and upward hydrometeor fluxes, but with weaker upward mass flux magnitudes, as in Hirt et al. (2020). This greater low-level leading-line ascent in 1-km simulations may also explain why the more focused linear structures of leading-line MCSs occurred in Thielen and Gallus (2019).

Somewhat similar trends were noted with WSM6 MP cold pool intensity-weighted areal coverage at the 75th percentile as with the Thompson MP simulations. Surface ($\theta'_{sfc}$) and total ($C_{total}$) cold pools generally expanded in size with time for all model grid spacings (Figs. 17a,d), though surface-based layer

and elevated cold pool areal coverage ($D_{sl}$, $C_{sl}$, $D_{elv}$, and $C_{elv}$) leveled off after t4 (Figs. 17b,c,e,f). As such, WSM6 MP cold pools were smaller than Thompson MP by about 10 000 km² for the last few sampled hours of MCS evolution. While finer $\Delta x$ and $\Delta z$ WSM6 MP $D_{sl}$ intensities and coverage were occasionally significantly greater than in runs with coarser grid spacing (Fig. 17b), WSM6 MP $C_{sl}$ values were more similar among grid spacings (Fig. 17e) compared to Thompson MP values. In the cold pool elevated layer, finer $\Delta x$ and $\Delta z$ runs had intensities and coverage of $D_{elv}$ and $C_{elv}$ significantly greater than in coarser runs from roughly t2 onward (Figs. 17c,f). With greater similarities between WSM6 MP grid spacings of both $C_{sl}$ and $C_{elv}$, it is not surprising to see that WSM6 MP $C_{total}$ cold pools are much more similar among varying grid spacings compared to Thompson MP cold pools.

However, Figs. 18a–m shows that higher rainwater and graupel mixing ratios, upward and downward mass fluxes, rainwater evaporation, melting graupel rates, and total microphysical latent cooling occur with relatively greater volumetric coverage in 1- versus 3-km runs employing either 50 or 100 vertical levels, as in Thompson MP runs. For WSM6 MP cold pools, rainwater evaporation and graupel melting dominate in volumetric coverage over melting snow by 2–4 times the number of grid points (Figs. 18i–l). Graupel and snow particles are larger in WSM6 MP runs than in Thompson MP, so they fall faster (Bao et al. 2019), lessening snow melting rates in finer $\Delta z$ runs with better resolved vertical layers. More graupel production and rainwater production for evaporation is favored, supporting a deeper, stronger, more widespread cold pool in finer $\Delta z$ runs. In addition, Figs. 18n–o shows that finer $\Delta x$ simulations supported greater areal coverage of stronger updraft intensities, with Fig. 16 (bottom) showing
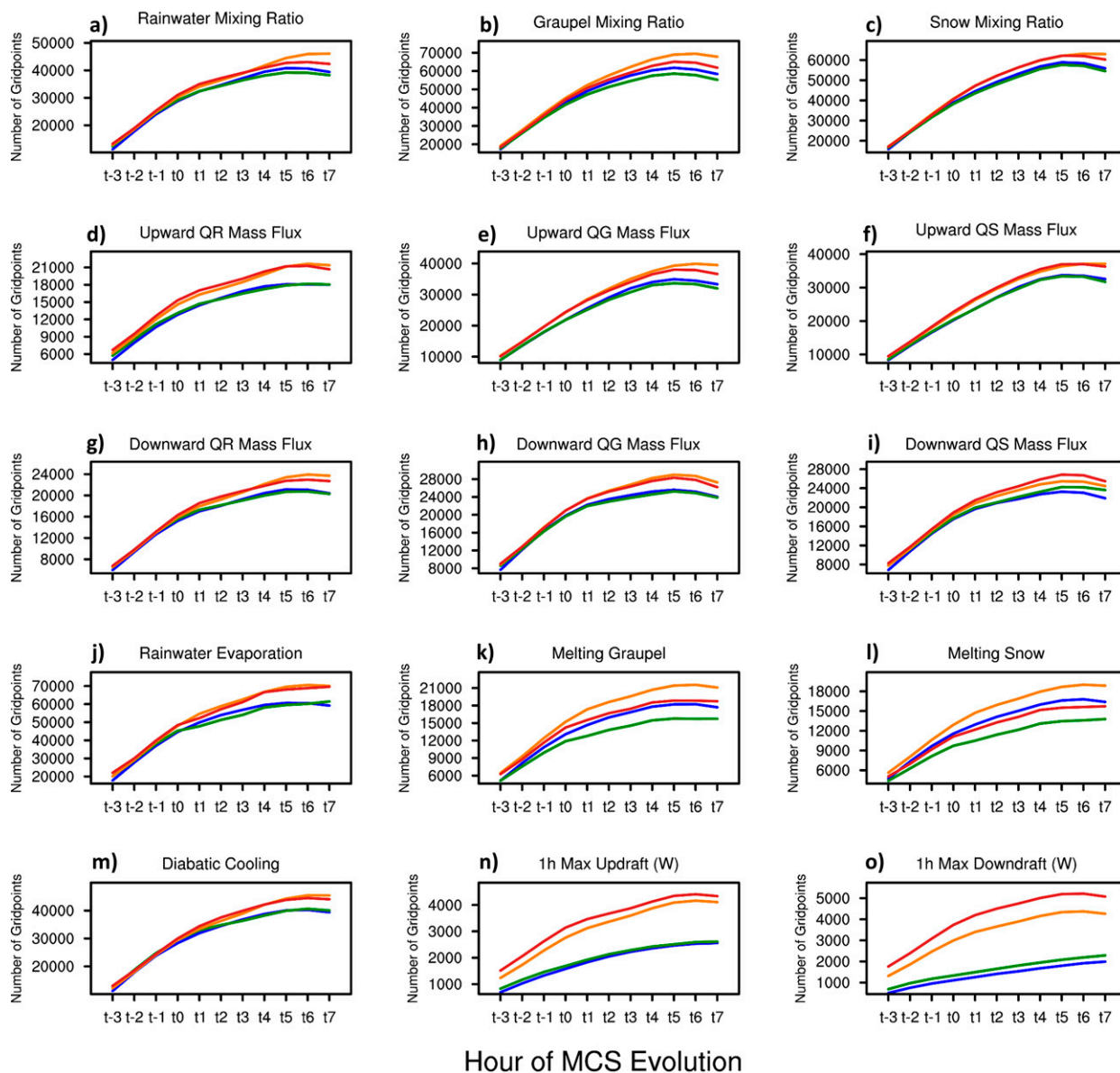
## WSM6 Scheme - 75th Percentile



FIG. 18. As in Fig. 14, but for WSM6 MP simulations.

significantly more 1-km midlevel updrafts than in 3-km runs. As exemplified in the 9 July 2020 case (Fig. 19), the primary physical driver for greater combined cold pool intensity and expanse in finer $\Delta x$ and $\Delta z$ runs appeared to be more abundant midlevel updrafts around $t - 2$ to t0 generating a stronger, more continuous leading-line of deep convection and a subsequent surface-based cold pool circulation, as seen in all the other cases when employing WSM6 MP. It is speculated that greater numbers of updrafts focused on the leading line generate more focused corridors of rearward advected

hydrometeors, serving as the source of greater graupel melting and rainwater evaporation and subsequently deeper, more expansive cold pools in finer $\Delta x$ and $\Delta z$ runs.

## 4. Summary and discussion

In total, 11 observed MCS cases were simulated with 3- and 1-km horizontal grid spacing while also employing 50 and 100 vertical levels on a stretched grid to gauge how refining $\Delta x$ and $\Delta z$ influenced MCS cold pool evolution. Simulations
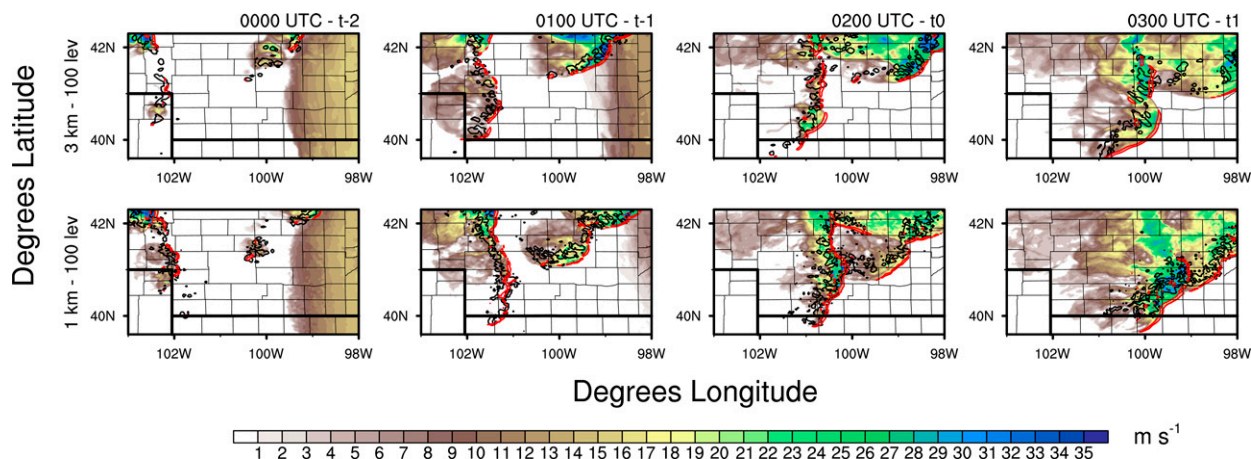
FIG. 19. As in Fig. 15, but for WSM6 MP simulations.

were conducted with both part double-moment (Thompson) and one-moment (WSM6) MP schemes to assess how impacts on cold pool characteristics from grid spacing changes might differ when switching schemes, and if the grid spacing changes were more influential than MP changes. Weaker but under-resolved updrafts supporting localized pockets of greater hydrometeor concentrations, coupled with better vertically resolved graupel and snow melting and rainwater evaporation processes (and resultant total latent microphysical cooling) are likely responsible for generating the strongest surface-based simulated cold pool magnitudes and depths employing $\Delta x = 3$ km grid spacing with 100 vertical levels in either Thompson or WSM6 MP runs. However, overall cold pool intensity was greater in runs with finer grid spacing, influenced by the expanse of greater cold pool depths and $C$ magnitudes driven by stronger, more abundant updrafts focused along the MCS leading line in both Thompson and WSM6 MP simulations. The greater number of midlevel updrafts in $\Delta x = 1$-km simulations supported a greater volumetric rearward advection of frozen hydrometeors along the convective leading line, supporting more widespread snow and graupel melting and rainwater evaporation to encourage further strengthening of the surface-based cold pool over a larger area. Finer $\Delta z$ augmented the cold pool further, and it is believed that better resolved frozen hydrometeor melting and rainwater evaporation processes is the cause for stronger, deeper cold pools in runs with 100 levels.

It is important to note that the sample size for this study was relatively small and that case-to-case variability existed in simulated MCS evolution. Simulated MCS cold pools for different cases often matured at different times relative to initiation, and some simulated MCSs matured through either the merging of smaller organized line segments, or the upscale growth of smaller deep convective clusters. The variability in MCS initiation methods can lead to large spread in cold pool depth and magnitudes among cases for a given spatial or MP configuration. This explains why cold pool magnitudes or depths under a given grid spacing or MP scheme could vary on the order of 10 m s$^{-1}$ or around 1 km while averages of

cold pool depths or intensities between grid spacings may vary by 1–10 m s$^{-1}$ or 100 m. This means that finer $\Delta x$ and $\Delta z$ simulations may support deeper, more expansive cold pools and MCSs, but these changes in MCS evolution may not be meteorologically meaningful. For example, it should not be expected that a simulated MCS should always go from a marginally organized squall line with $\Delta x = 3$ km to a highly organized bow echo in 1-km runs. Nonetheless, it is also important to examine how $\Delta x$ and $\Delta z$ influences MCS placement and timing as well as QPF performance relative to observations, which are addressed in Part II of this study.

Given the highly varying nature of the updraft and associated graupel cores, it was extremely difficult to explicitly show details of graupel tendencies through the MCS life cycle for any of the 11 cases without "cherry-picking" the analyses for favorable results, especially for WSM6 MP simulations. As such, only inferences were made on how graupel sizes, fall speeds, and melting with changing $\Delta x$ or $\Delta z$ accelerated WSM6 MP cold pool life cycles based on tendencies for WSM6 MP storm cores to become graupel loaded. A need exists to evaluate individual microphysical tendencies and their latent cooling rates in a more simplified environment to solidify the findings in this work, and this could be done in an idealized framework employing CM1 (as in Mallinson and Lasher-Trapp 2019). Improved understanding of MP behavior could facilitate model physics improvements that have been argued would be one of the more effective ways of improving convection-allowing forecasts (Potvin et al. 2017).

microphysical tendencies. The authors would also like to thank the editor and three anonymous peer reviewers for their diligent efforts in evaluating this paper and providing valuable feedback, leading to a substantially improved manuscript.

*Data availability statement.* The WRF output that supports the findings of this work are available in DataShare, Iowa State's open research data repository. All other data availability locations are as defined in text and within the references of this manuscript.

## REFERENCES

Adams-Selin, R. D., S. C. van den Heever, and R. H. Johnson, 2013a: Sensitivity of bow-echo simulation to microphysical parameterizations. *Wea. Forecasting*, **28**, 1188–1209, https://doi.org/10.1175/WAF-D-12-00108.1.

——, ——, and ——, 2013b: Impact of graupel parameterization schemes on idealized bow echo simulations. *Mon. Wea. Rev.*, **141**, 1241–1262, https://doi.org/10.1175/MWR-D-12-00064.1.

Bao, J.-W., S. A. Michelson, and E. D. Grell, 2019: Microphysical process comparison of three microphysics parameterization schemes in the WRF Model for an idealized squall-line case study. *Mon. Wea. Rev.*, **147**, 3093–3120, https://doi.org/10.1175/MWR-D-18-0249.1.

Betts, A. K., 1976: The thermodynamic transformation of the tropical subcloud layer by precipitation and downdrafts. *J. Atmos. Sci.*, **33**, 1008–1020, https://doi.org/10.1175/1520-0469(1976)033<1008:TTTOTT>2.0.CO;2.

Billings, J. M., and M. D. Parker, 2012: Evolution and maintenance of the 22–23 June 2003 nocturnal convection during BAMEX. *Wea. Forecasting*, **27**, 279–300, https://doi.org/10.1175/WAF-D-11-00056.1.

Borque, P., S. W. Nesbitt, R. J. Trapp, S. Lasher-Trapp, and M. Oue, 2020: Observational study of the thermodynamics and morphological characteristics of a midlatitude continental cold pool event. *Mon. Wea. Rev.*, **148**, 719–737, https://doi.org/10.1175/MWR-D-19-0068.1.

Braun, S. A., and R. A. Houze Jr., 1995: Melting and freezing in a mesoscale convective system. *Quart. J. Roy. Meteor. Soc.*, **121**, 55–77, https://doi.org/10.1002/qj.49712152104.

Bryan, G. H., and R. Rotunno, 2008: Gravity currents in a deep anelastic atmosphere. *J. Atmos. Sci.*, **65**, 536–556, https://doi.org/10.1175/2007JAS2443.1.

——, and H. Morrison, 2012: Sensitivity of a simulated squall line to horizontal resolution and parameterization of microphysics. *Mon. Wea. Rev.*, **140**, 202–225, https://doi.org/10.1175/MWR-D-11-00046.1.

——, J. C. Wyngaard, and J. M. Fritsch, 2003: Resolution requirements for the simulation of deep moist convection. *Mon. Wea. Rev.*, **131**, 2394–2416, https://doi.org/10.1175/1520-0493(2003)131<2394:RRFTSO>2.0.CO;2.

Caniaux, G., J.-L. Redelsperger, and J.-P. Lafore, 1994: A numerical study of the stratiform region of a fast-moving squall line. Part I: General description and water and heat budgets. *J. Atmos. Sci.*, **51**, 2046–2074, https://doi.org/10.1175/1520-0469(1994)051<2046:ANSOTS>2.0.CO;2.

Charba, J., 1974: Application of gravity current model to analysis of squall-line gust front. *Mon. Wea. Rev.*, **102**, 140–156, https://doi.org/10.1175/1520-0493(1974)102<0140:AOGCMT>2.0.CO;2.

Chen, F., and J. Dudhia, 2001: Coupling an advanced land surface-hydrology model with the Penn State–NCAR MM5 Modeling System. Part I: Model implementation and sensitivity. *Mon. Wea. Rev.*, **129**, 569–585, https://doi.org/10.1175/1520-0493(2001)129<0569:CAALSH>2.0.CO;2.

CISL, 2020: Cheyenne: HPE/SGI ICE XA System (University Community Computing). National Center for Atmospheric Research, accessed 13 June 2022, https://doi.org/10.5065/D6RX99HX.

Clark, A. J., and Coauthors, 2012: An overview of the 2010 Hazardous Weather Testbed Experimental Forecast Program Spring Experiment. *Bull. Amer. Meteor. Soc.*, **93**, 55–74, https://doi.org/10.1175/BAMS-D-11-00040.1.

Coniglio, M. C., and D. J. Stensrud, 2001: Simulation of a progressive derecho using composite initial conditions. *Mon. Wea. Rev.*, **129**, 1593–1616, https://doi.org/10.1175/1520-0493(2001)129<1593:SOAPDU>2.0.CO;2.

——, ——, and L. J. Wicker, 2006: Effects of upper-level shear on the structure and maintenance of strong quasi-linear mesoscale convective systems. *J. Atmos. Sci.*, **63**, 1231–1252, https://doi.org/10.1175/JAS3681.1.

——, J. Y. Hwang, and D. J. Stensrud, 2010: Environmental factors in the upscale growth and longevity of MCSs derived from the Rapid Update Cycle analyses. *Mon. Wea. Rev.*, **138**, 3514–3539, https://doi.org/10.1175/2010MWR3233.1.

Corfidi, S. F., 2003: Cold pools and MCS propagation: Forecasting the motion of downwind-developing MCSs. *Wea. Forecasting*, **18**, 997–1017, https://doi.org/10.1175/1520-0434(2003)018<0997:CPAMPF>2.0.CO;2.

——, J. H. Merritt, and J. M. Fritsch, 1996: Predicting the movement of mesoscale convective complexes. *Wea. Forecasting*, **11**, 41–46, https://doi.org/10.1175/1520-0434(1996)011<0041:PTMOMC>2.0.CO;2.

Davis, C., B. Brown, and R. Bullock, 2006a: Object-based verification of precipitation forecasts. Part I: Methods and application to mesoscale rain areas. *Mon. Wea. Rev.*, **134**, 1772–1784, https://doi.org/10.1175/MWR3145.1.

——, ——, and ——, 2006b: Object-based verification of precipitation forecasts. Part II: Application to convective rain systems. *Mon. Wea. Rev.*, **134**, 1785–1795, https://doi.org/10.1175/MWR3146.1.

Done, J., C. A. Davis, and M. Weisman, 2004: The next generation of NWP: Explicit forecasts of convection using the Weather Research and Forecasting (WRF) Model. *Atmos. Sci. Lett.*, **5**, 110–117, https://doi.org/10.1002/asl.72.

Droegemeier, K. K., and R. B. Wilhelmson, 1987: Numerical simulation of thunderstorm outflow dynamics. Part I: Outflow sensitivity experiments and turbulence dynamics. *J. Atmos. Sci.*, **44**, 1180–1210, https://doi.org/10.1175/1520-0469(1987)044<1180:NSOTOD>2.0.CO;2.

Dudhia, J., 1989: Numerical study of convection observed during the Winter Monsoon Experiment using a mesoscale two-dimensional model. *J. Atmos. Sci.*, **46**, 3077–3107, https://doi.org/10.1175/1520-0469(1989)046<3077:NSOCOD>2.0.CO;2.

——, M. W. Moncrieff, and D. W. K. So, 1987: The two-dimensional dynamics of West African squall lines. *Quart. J. Roy. Meteor. Soc.*, **113**, 121–146, https://doi.org/10.1002/qj.49711347508.

Fan, J., and Coauthors, 2017: Cloud-resolving model intercomparison of an MC3E squall line case: Part I—Convective updrafts. *J. Geophys. Res. Atmos.*, **122**, 9351–9378, https://doi.org/10.1002/2017JD026622.

Field, P. R., A. J. Heymsfield, A. G. Detwiler, and J. M. Wilkinson, 2019: Normalized hail particle size distributions from the T-28 storm-penetrating aircraft. *J. Atmos. Meteor. Climatol.*, **58**, 231–245, https://doi.org/10.1175/JAMC-D-18-0118.1.

Fovell, R. G., and Y. Ogura, 1988: Numerical simulation of a mid-latitude squall line in two dimensions. *J. Atmos. Sci.*, **45**, 3846–3879, https://doi.org/10.1175/1520-0469(1988)045<3846:NSOAMS>2.0.CO;2.

Fujita, T., 1959: Precipitation and cold air production in mesoscale thunderstorm systems. *J. Atmos. Sci.*, **16**, 454–466, https://doi.org/10.1175/1520-0469(1959)016<0454:PACAPI>2.0.CO;2.

Gallus, W. A., Jr., and R. H. Johnson, 1995a: The dynamics of circulations within the trailing stratiform region of squall lines. Part I: The 10–11 June PRE-STORM system. *J. Atmos. Sci.*, **52**, 2161–2187, https://doi.org/10.1175/1520-0469(1995)052<2161:TDOCWT>2.0.CO;2.

——, and ——, 1995b: The dynamics of circulations within the trailing stratiform regions of squall lines. Part II: Influence of the convective line and ambient environment. *J. Atmos. Sci.*, **52**, 2188–2211, https://doi.org/10.1175/1520-0469(1995)052<2188:TDOCWT>2.0.CO;2.

——, N. A. Snook, and E. V. Johnson, 2008: Spring and summer severe weather reports over the Midwest as a function of convective mode: A preliminary study. *Wea. Forecasting*, **23**, 101–113, https://doi.org/10.1175/2007WAF2006120.1.

Grim, J. A., G. M. McFarquhar, R. M. Rauber, A. M. Smith, and B. F. Jewett, 2009: Microphysical and thermodynamic structure and evolution of the trailing stratiform regions of mesoscale convective systems during BAMEX. Part II: Column model simulations. *Mon. Wea. Rev.*, **137**, 1186–1205, https://doi.org/10.1175/2008MWR2505.1.

Hirt, M., G. C. Craig, S. A. K. Schäfer, J. Savre, and R. Heinze, 2020: Cold-pool-driven convective initiation: Using causal graph analysis to determine what convection-permitting models are missing. *Quart. J. Roy. Meteor. Soc.*, **146**, 2205–2227, https://doi.org/10.1002/qj.3788.

Hong, S.-Y., and J.-O. J. Lim, 2006: The WRF single-moment 6-class microphysics scheme (WSM6). *J. Korean Meteor. Soc.*, **42**, 129–151.

Iowa Environmental Mesonet, 2020: Documentation on IEM generated NEXRAD Mosaics. Iowa State University, accessed 22 October 2020, https://mesonet.agron.iastate.edu/docs/nexrad_composites/.

James, R., J. Fritsch, and P. M. Markowski, 2005: Environmental distinctions between cellular and slabular convective lines. *Mon. Wea. Rev.*, **133**, 2669–2691, https://doi.org/10.1175/MWR3002.1.

Janjić, Z. I., 1994: The step-mountain eta coordinate model: Further developments of the convection, viscous sublayer, and turbulence closure schemes. *Mon. Wea. Rev.*, **122**, 927–945, https://doi.org/10.1175/1520-0493(1994)122<0927:TSMECM>2.0.CO;2.

Kain, J. S., and Coauthors, 2008: Some practical considerations regarding horizontal resolution in the first generation of operational convection-allowing NWP. *Wea. Forecasting*, **23**, 931–952, https://doi.org/10.1175/WAF2007106.1.

Lafore, J.-P., and M. W. Moncrieff, 1989: A numerical investigation of the organization and interaction of the convective and stratiform regions of tropical squall lines. *J. Atmos. Sci.*, **46**, 521–544, https://doi.org/10.1175/1520-0469(1989)046<0521:ANIOTO>2.0.CO;2.

Leary, C. A., and R. A. Houze Jr., 1979: Melting and evaporation of hydrometeors in precipitation from the anvil clouds of deep tropical convection. *J. Atmos. Sci.*, **36**, 669–679, https://doi.org/10.1175/1520-0469(1979)036<0669:MAEOHI>2.0.CO;2.

Lebo, Z. J., and H. Morrison, 2015: Effects of horizontal and vertical grid spacing on mixing in simulated squall lines and implications for convective strength and structure. *Mon. Wea. Rev.*, **143**, 4355–4375, https://doi.org/10.1175/MWR-D-15-0154.1.

Li, X., W.-K. Tao, A. P. Khain, J. Simpson, and D. E. Johnson, 2009a: Sensitivity of a cloud-resolving model to bulk and explicit bin microphysical schemes. Part I: Comparisons. *J. Atmos. Sci.*, **66**, 3–21, https://doi.org/10.1175/2008JAS2646.1.

——, ——, ——, J. Shimpson, and D. E. Johnson, 2009b: Sensitivity of a cloud-resolving model to bulk and explicit bin microphysical schemes. Part II: Cloud microphysics and storm dynamics interactions. *J. Atmos. Sci.*, **66**, 22–40, https://doi.org/10.1175/2008JAS2647.1.

Mallinson, H. M., and S. G. Lasher-Trapp, 2019: An investigation of hydrometeor latent cooling upon convective cold pool formation, sustainment, and properties. *Mon. Wea. Rev.*, **147**, 3205–3222, https://doi.org/10.1175/MWR-D-18-0382.1.

Markowski, M., and Y. Richardson, 2010: *Mesoscale Meteorology in Midlatitudes*. John Wiley and Sons, 407 pp.

Marsham, J. H., S. B. Trier, T. M. Weckwerth, and J. W. Wilson, 2011: Observations of elevated convection initiation leading to a surface-based squall line during 13 June IHOP_2002. *Mon. Wea. Rev.*, **139**, 247–271, https://doi.org/10.1175/2010MWR3422.1.

Mendenhall, W., and T. Sincich, 2007: *Statistics for Engineering and the Sciences.* 5th ed. Pearson-Prentice Hall, 1060 pp.

Miller, M. J., and A. K. Betts, 1977: Traveling convective storms over Venezuela. *Mon. Wea. Rev.*, **105**, 833–848, https://doi.org/10.1175/1520-0493(1977)105<0833:TCSOV>2.0.CO;2.

Miller, R. L., C. L. Ziegler, and M. I. Biggerstaff, 2020: Seven-Doppler radar and in situ analysis of the 25–26 June 2015 Kansas MCS during PECAN. *Mon. Wea. Rev.*, **148**, 211–240, https://doi.org/10.1175/MWR-D-19-0151.1.

Mlawer, E. J., S. J. Taubman, P. D. Brown, M. J. Iacono and S. A. Clough, 1997: Radiative transfer for inhomogeneous atmospheres: RRTM, a validated correlated-k model for the longwave. *J. Geophys. Res.*, **102**, 16663–16682, https://doi.org/10.1029/97JD00237.

Newton, C. W., 1950: Structure and mechanism of the pre-frontal squall line. *J. Meteor.*, **7**, 210–222, https://doi.org/10.1175/1520-0469(1950)007<0210:SAMOTP>2.0.CO;2.

——, and J. C. Fankhauser, 1975: Movement and propagation of multicellular convective storms. *Pure Appl. Geophys.*, **113**, 747–764, https://doi.org/10.1007/BF01592957.

NOAA/NCDC, 2015: NCEP Numerical Weather Prediction Models North American Meso-Scale Grid 218. Subset used: June 2015–July 2020, accessed August 2020, ftp://ftp.arl.noaa.gov/pub/archives/nam12.

Parker, M. D., 2008: Response of simulated squall lines to low-level cooling. *J. Atmos. Sci.*, **65**, 1323–1341, https://doi.org/10.1175/2007JAS2507.1.

——, 2021: Self-organization and maintenance of simulated nocturnal mesoscale convective systems from PECAN. *Mon. Wea. Rev.*, **149**, 999–1022, https://doi.org/10.1175/MWR-D-20-0263.1.

——, and R. H. Johnson, 2000: Organizational modes of midlatitude mesoscale convective systems. *Mon. Wea. Rev.*, **128**, 3413–3436, https://doi.org/10.1175/1520-0493(2001)129<3413:OMOMMC>2.0.CO;2.

——, B. S. Borchardt, R. L. Miller, and C. L. Ziegler, 2020: Simulated evolution and severe wind production by the 25–26 June 2015 nocturnal MCS from PECAN. *Mon. Wea. Rev.*, **148**, 183–209, https://doi.org/10.1175/MWR-D-19-0072.1.

Peters, K., and C. Hohenegger, 2017: On the dependence of squall-line characteristics on surface conditions. *J. Atmos. Sci.*, **74**, 2211–2228, https://doi.org/10.1175/JAS-D-16-0290.1.

Potvin, C. K., E. M. Murillo, M. L. Flora, and D. M. Wheatley, 2017: Sensitivity of supercell simulations to initial-condition resolution. *J. Atmos. Sci.*, **74**, 5–26, https://doi.org/10.1175/JAS-D-16-0098.1.

Rotunno, R., J. B. Klemp, and M. L. Weisman, 1988: A theory for strong, long-lived squall lines. *J. Atmos. Sci.*, **45**, 463–485, https://doi.org/10.1175/1520-0469(1988)045<0463:ATFSLL>2.0.CO;2.

Rutledge, S. A., 1986: Diagnostic modeling study of the stratiform region associated with a tropical squall line. *J. Atmos. Sci.*, **43**, 1356–1378, https://doi.org/10.1175/1520-0469(1986)043<1356:ADMSOT>2.0.CO;2.

——, and R. A. Houze Jr., 1987: A diagnostic modeling study of the trailing stratiform region of a midlatitude squall line. *J. Atmos. Sci.*, **44**, 2640–2656, https://doi.org/10.1175/1520-0469(1987)044<2640:ADMSOT>2.0.CO;2.

Skamarock, W. C., and Coauthors, 2008: A description of the Advanced Research WRF version 3. NCAR Tech. Note NCAR/TN-475+STR, 113 pp., https://doi.org/10.5065/D68S4MVH.

——, and Coauthors, 2019a: A description of the Advanced Research WRF Model version 4. NCAR Tech. Note NCAR/TN-556+STR, 145 pp., https://doi.org/10.5065/1dfh-6p97.

——, C. Snyder, J. B. Klemp, and S.-H. Park, 2019b: Vertical resolution requirements in atmospheric simulation. *Mon. Wea. Rev.*, **147**, 2641–2656, https://doi.org/10.1175/MWR-D-19-0043.1.

Smith, T. M., and Coauthors, 2016: Multi-Radar Multi-Sensor (MRMS) severe weather and aviation products: Initial operating capabilities. *Bull. Amer. Meteor. Soc.*, **97**, 1617–1630, https://doi.org/10.1175/BAMS-D-14-00173.1.

Squitieri, B. J., and W. A. Gallus Jr., 2020: On the forecast sensitivity of MCS cold pools and related features to horizontal grid spacing in convection-allowing WRF simulations. *Wea. Forecasting*, **35**, 325–346, https://doi.org/10.1175/WAF-D-19-0016.1.

——, and ——, 2022: On the changes in convection-allowing WRF forecasts of MCS evolution due to decreases in model horizontal and vertical grid spacing. Part II: Impacts on QPFs. *Wea. Forecasting*, **37**, 1925–1940, https://doi.org/10.1175/WAF-D-22-0042.1.

Thielen, J. E., and W. A. Gallus Jr., 2019: Influences of horizontal grid spacing and microphysics on WRF forecasts of convective morphology evolution for nocturnal MCSs in weakly forced environments. *Wea. Forecasting*, **34**, 1495–1517, https://doi.org/10.1175/WAF-D-18-0210.1.

Thompson, G., P. R. Field, R. M. Rasmussen, and W. D. Hall, 2008: Explicit forecasts of winter precipitation using an improved bulk microphysics scheme. Part II: Implementation of a new snow parameterization. *Mon. Wea. Rev.*, **136**, 5095–5115, https://doi.org/10.1175/2008MWR2387.1.

Tuttle, J. D., and R. E. Carbone, 2004: Coherent regeneration and the role of water vapor and shear in a long-lived convective episode. *Mon. Wea. Rev.*, **132**, 192–208, https://doi.org/10.1175/1520-0493(2004)132<0192:CRATRO>2.0.CO;2.

Van Weverberg, K., A. M. Vogelmann, H. Morrison, and J. A. Milbrandt, 2012: Sensitivity of idealized squall-line simulations to the level of complexity used in two-moment bulk microphysics schemes. *Mon. Wea. Rev.*, **140**, 1883–1907, https://doi.org/10.1175/MWR-D-11-00120.1.

Verrelle, A., D. Ricard, and C. Lac, 2015: Sensitivity of high-resolution idealized simulations of thunderstorms to horizontal resolution and turbulence parameterization. *Quart. J. Roy. Meteor. Soc.*, **141**, 433–448, https://doi.org/10.1002/qj.2363.

Weisman, M. L., 1992: The role of convectively generated rear-inflow jets in the evolution of long-lived mesoconvective systems. *J. Atmos. Sci.*, **49**, 1826–1847, https://doi.org/10.1175/1520-0469(1992)049<1826:TROCGR>2.0.CO;2.

——, C. Davis, W. Wang, K. W. Manning, and J. B. Klemp, 2008: Experiences with 0–36-h explicit convective forecasts with the WRF-ARW Model. *Wea. Forecasting*, **23**, 407–437, https://doi.org/10.1175/2007WAF2007005.1.

Werner, K., and UCAR, 2020: WRF version 4.2. Accessed August 2020, https://github.com/wrf-model/WRF/releases.

Wilhelmson, R. B., and C.-S. Chen, 1982: A simulation of the development of successive cells along a cold outflow boundary. *J. Atmos. Sci.*, **39**, 1466–1483, https://doi.org/10.1175/1520-0469(1982)039<1466:ASOTDO>2.0.CO;2.

Zipser, E. J., 1982: Use of a conceptual model of the life cycle of mesoscale convective systems to improve very-short-range forecasts. *Nowcasting*, 1st ed. K. Browning, Ed., Academic Press, 191–204.